

A Search for Gravitationally Lensed Quasars and Quasar Pairs in Pan-STARRS1: Spectroscopy and Sources of Shear in the Diamond 2M1134–2103

Cristian E. Rusu,^{1*} Ciprian T. Berghea,² Christopher D. Fassnacht,³
Anupreeta More,^{4,5} Erica Seman,² George J. Nelson² and Geoff C.-F. Chen³

¹Subaru Telescope, National Astronomical Observatory of Japan, 650 N Aohoku Pl, Hilo, HI 96720

²U.S. Naval Observatory (USNO), 3450 Massachusetts Avenue NW, Washington, DC 20392, USA

³Department of Physics, University of California, Davis, CA 95616, USA

⁴Kavli IPMU (WPI), UTIAS, The University of Tokyo, Kashiwa, Chiba 277-8583, Japan

⁵Inter-University Centre for Astronomy and Astrophysics, Post Bag 4, Ganeshkhind, Pune 410007, India

Accepted XXX. Received YYY; in original form ZZZ

ABSTRACT

We present results of a systematic search for gravitationally lensed quasars in Pan-STARRS1. Our final sample of candidates comprises of 91 systems, not including 25 rediscovered lensed quasars and quasar pairs. In the absence of spectroscopy to verify the lensing nature of the candidates, the main sources of contaminants are likely to be quasar pairs, which we consider to be a byproduct of our work, and a smaller number of quasar+star associations. Amongst the independently discovered quads is 2M1134–2103, for which we obtained spectroscopy for the first time, finding a redshift of 2.77 for the quasar. There is evidence for microlensing in at least one image. We perform detailed mass modeling of this system using archival imaging data, and find that the unusually large shear responsible for the diamond-like configuration can be attributed mainly to a faint companion $\sim 4''$ away, and to a galaxy group/cluster $\sim 30''$ away. We also set limits of $z \sim 0.5 - 1.5$ on the redshift of the lensing galaxy, based on its brightness, the image separation of the lensed images, and an analysis of the observed photometric flux ratios.

Key words: gravitational lensing; strong – quasars: individual: 2M1134–2103

1 INTRODUCTION

To date, ~ 60 quadruple (quad) and ~ 200 double gravitationally lensed quasars have been discovered¹. Their value as probes of cosmology and astrophysics has been explored observationally for the past four decades (e.g., see reviews by Claeskens & Surdej 2002; Treu & Marshall 2016), yet their number is still a limiting factor for many focused studies (e.g., Oguri et al. 2012; Schechter et al. 2014; Bonvin et al. 2017). We are currently in a post-Sloan Digital Sky Survey (SDSS; York et al. 2000) era when the large ongoing imaging surveys such as the Panoramic Survey Telescope and Rapid Response

System (Pan-STARRS1, hereafter PS1; Chambers et al. 2016), the Dark Energy Survey (Flaugher et al. 2015) and the Hyper Suprime-Cam Subaru Strategic Program (Aihara et al. 2018) do not (yet) have a spectroscopic counterpart, making it difficult to identify lensed quasars. As a result, contemporary dedicated searches for lensed quasars rely on selecting their candidates by applying machine learning techniques such as artificial neural networks (e.g., Agnello et al. 2015) or gaussian mixture models (e.g., Ostrovski et al. 2017; Williams, Agnello, & Treu 2017) to multi-filter photometric catalogues in conjunction with pixel-by-pixel pattern recognition; by looking for flux and position offsets between these surveys and *Gaia* (e.g., Lemon et al. 2017; Agnello & Spiniello 2018), including capitalizing on the superior *Gaia* resolution to resolve blended sources (e.g., Lemon et al. 2018; Agnello et al. 2018,c; Delchambre et al. 2019) and combining multiple such methods (e.g., Spiniello et al. 2018; Lemon, Auger, & McMahon 2019); by assessing the

* Subaru Fellow; e-mail: cerusu@naoj.org

¹ Lemon, Auger, & McMahon (2019) have compiled an up-to-date list of known lensed quasars, maintained at <https://www.ast.cam.ac.uk/boa/research/lensedquasars/>. Also, C. Lemon, private communication.

plausibility of valid lensing configurations on automatically detected sources (e.g., [Chan et al. 2015](#)); and/or by complementing these with variability information (e.g., [Berghea et al. 2017](#); [Kostrzewa-Rutkowska et al. 2018](#)).

Encouraged by the serendipitous discovery by [Berghea et al. \(2017\)](#) of the first quad from PS1, PSOJ0147, we have begun a systematic search for lensed quasars in this survey, by cross-correlating sources with the parent AGN catalogue of [Secrest et al. \(2015\)](#). As the first PS1 data was released in December 2016, mining it for lensed quasars has only recently begun (e.g., [Ostrovski et al. 2018](#)), making it likely that other lensed quasars, including bright, large separation quads, are yet to be found. Given the PS1 sky coverage and depth, [Oguri & Marshall \(2010\)](#) estimate that PS1 contains ~ 2000 lensed quasars, including 300 quads.

Recently, [Lucey et al. \(2018, hereafter L18\)](#) have announced the discovery of a new bright, large-separation quad, 2M1134–2103. This was a serendipitous discovery, as part of a search for extended 2MASS ([Skrutskie et al. 1997](#)) sources in the PS1 footprint, to include as targets for the Taipan Galaxy Survey ([da Cunha et al. 2017](#)). As part of our search, we have independently discovered this system. Here, we aim to present a more in-depth modeling of the archival imaging data, looking in particular to identify the cause for the unusually large shear inferred in L18. In addition, we present for the first time spectroscopic data for this system.

The structure of this paper is as follows: in Section 2 we describe our search technique and a new sample of lensed quasars and quasar pair candidates. In Section 3 we describe our analysis of the archival imaging data of 2M1134–2103, and in Section 4 our newly acquired spectroscopic data. In Section 5 we present our mass modeling of 2M1134–2103, and provide plausible explanations for the unusually large shear. We conclude in Section 6. Where necessary, we use a flat cosmology with $\Omega_{\Lambda} = 0.74$ and $h = 0.72$.

2 A SEARCH FOR GRAVITATIONALLY LENSED QUASARS IN PS1

2.1 Selection based on catalogue cuts and visual inspection

PS1 is a wide-field imaging system with a 1.8 m telescope and 7.7 deg² field of view, located on the summit of Haleakala in the Hawaiian island of Maui. The 1.4 Gpixel camera consists of 60 CCDs with pixel size of 0.256 arcsec ([Onaka & al. 2008](#); [Tonry & Onaka 2008](#)). The first PS1 data release includes both images and a photometry catalogue ([Chambers et al. 2016](#)). PS1 uses five SDSS-like filters (g_{P1} , r_{P1} , i_{P1} , z_{P1} , y_{P1}). The largest survey PS1 performs is the 3 π survey, covering the entire sky north of -30 deg declination.

As we did for PSOJ0147, we start our search with the AGN candidates catalog of [Secrest et al. \(2015\)](#), based on two mid-infrared colors measured with the *Wide-field Infrared Survey Explorer* (*WISE*; [Wright et al. 2010](#)). We cross-correlate this catalog with the PS1 catalog² ([Flewelling et al. 2016](#)) using a 3'' radius cone search and

keep 79951 candidates which have at least two counterparts (step *i*). Next, we remove candidates within 15 degrees of the galactic plane, resulting in 64055 remaining sources (*ii*). We then impose a faint magnitude cut of $i = 19.5$ on the closest counterpart, in order to eliminate spurious candidates. This results in 25493 sources remaining (*iii*)³. Finally, we impose that the two brightest sources in each system should be similar in color, removing the ones with $g - i$ differences larger than 1.5 mag and $i - y$ differences larger than 1.0 mag (*iv*). The final sample contains 18015 candidates.

We chose these cuts in order to recover most of the known lenses at the intersection of PS1 and the [Secrest et al. \(2015\)](#) catalogue, while resulting in a number of candidates small enough to allow visual inspection. From an all-sky catalogue of ~ 260 known lenses ([Lemon, Auger, & McMahon 2019](#)), which we matched with the [Secrest et al. \(2015\)](#) catalogue to insure a match within 10'', we found 45 lenses for which their [Secrest et al. \(2015\)](#) catalogue counterparts have at least 2 detections in PS1 within 3'' (corresponding to step *i*). These are further reduced to 44 (step *ii*), 32 (*iii*), and 30 lenses (*iv*)⁴. In addition to the cross-match with the known catalogue of lensed quasars, we also looked for previously known non-lens systems, by cross-matching the coordinates of our candidates with the list of known sources from the SIMBAD Astronomical Database⁵ and the NASA/IPAC Extragalactic Database⁶.

We downloaded 30'' \times 30'' postage stamp color JPEG images of the candidates using the PS1 cutout service⁷, which were then inspected visually by three of the authors (CTB, ES and GJN). Pairs with separation \lesssim a few arcsec between components (consistent with strong lensing by galaxies) and similar colors, triplets with a redder inner component, as well as quads with configurations consistent with canonical lensing configurations were kept. Finally, another three authors (CER, AM and GCFC) graded the remaining sample of 448 candidates. As is customary in the lens search community, they used the following grading system: 0: unlikely to be a lens; 1: possibly a lens candidate (satisfies only some criteria to be a lens); 2: probably a lens candidate (satisfies most criteria to be a lens); 3: almost certainly a lens (there is almost no doubt that this is a lens). We find 312 systems with an average grade ≥ 1 , and discard the rest.

Out of the 312 candidates, we recover a total of 15 known lenses. Of these, 6 are quads: PS J0147+4630 ([Berghea et al. 2017](#)), 2M 1134-2103 ([Lucey et al. 2018](#)), SDSS J1433+6007 ([Agnello et al. 2018a](#)), GraL J1537-3010 ([Lemon, Auger, & McMahon 2019](#);

<http://vizier.u-strasbg.fr/viz-bin/VizieR>, which contains fewer contaminants

³ Following step *iii*, we explored using an additional step to eliminate globular clusters and similar crowded regions, by imposing the condition that there are no more than seven counterparts within 10'' radius. This would have eliminated only 182 systems, all of which we have explored visually, making this step unnecessary.

⁴ In addition to these, two other lensed quasars survive our selection and grading process, but are not picked up by the cross-match with the catalogue of lenses because of differences in the reported coordinates: SDSS J1320+1644 and SDSS J1433+6007.

⁵ <http://simbad.u-strasbg.fr/simbad/sim-fcoo>

⁶ <http://ned.ipac.caltech.edu/?q=nearposn>

⁷ http://hla.stsci.edu/fitscutcgi_interface.html

² We use the version available on Vizier,

Delchambre et al. 2019), PS J1606-2333 (Lemon et al. 2018) and PS J1721+8842 (Lemon et al. 2018), and 9 are doubles: DES J0245-0556 (Agnello et al. 2018), PS J0259-2338 (Lemon et al. 2018), HE 1104-1805 (Wisotzki et al. 1993), J1206-2543 (Lemon et al. in prep.), SDSS J1206+4332 (Oguri et al. 2005), SDSS J1320+1644 (Rusu et al. 2013), ULAS J1405+0959 (Jackson et al. 2012), SDSS J1515+1511 (Inada et al. 2014), and J2212+3144 (Lemon, Auger, & McMahon 2019). This means that at the grading stage we miss the cluster quad SDSS J1004+4112 (Inada et al. 2003). In addition, at the initial visual inspection stage to produce the list for grading we miss the quad PG1115+080 (Weymann et al. 1980) and 15 doubles: PS J0028+0631 (Lemon et al. 2018), J0102+2445 (Lemon, Auger, & McMahon 2019), Q0142-100 (Surdej et al. 1987), PS J0949+4208 (Lemon et al. 2018), SDSS J1001+5027 (Oguri et al. 2005), SDSS J1313+5151 (Ofek et al. 2007), SDSS J1349+1227 (Kayo et al. 2010), SDSS J1442+4055 (More et al. 2016), ULAS J1527+0141 (Jackson et al. 2012), PS J2124+1632 (Lemon et al. 2018), another double from Ostrovski et al. in prep. and four more doubles from Lemon et al. in prep.

Our cross-match with known lenses shows that we are more efficient at recovering quads than doubles, which is to be expected, because typical quad configurations are easier to identify visually. We are also biased against large-separation lenses, due to our requirement to have at least two components within $3''$. Since at the visual selection stage we miss 17/32 of the known lenses included in our cutouts, we expect the completeness of our sample of candidates, defined as the ratio of the number of gravitational lenses in the final sample to the true number of lenses in the cutouts, to be $\lesssim 50\%$. Most of these are missed at the initial visual inspection stage. This can be attributed to two factors: first, most of the missed systems are doubles with only two clearly visible components in the cutouts, and with noticeable color differences between the components. On the other hand, the authors who have inspected the 18015 candidates have no formal experience with gravitational lenses. When the authors with formal experience graded 11/17 missed lenses, 9 of these received an average grade ≥ 1 .

We note that other known quads with bright lensing galaxies, such as 2M1310-1714 (L18), are not included in our sample because the lens light contaminates the infrared colors that the Secrest et al. (2015) AGN catalog is based on. Secrest et al. (2015) note that the chance of misclassifying stars in the AGN catalogue is $\leq 0.041\%$, so we expect that the main contaminants to our list of candidates, after visual examination, will be quasar + star pairs as well as quasar pairs, as either physically associated binary quasars or projected chance alignments. Indeed, 93 of our candidates, the great majority of those with spectroscopic results in the literature, consist of at least one AGN.

We note that we have typically given a grade of 1 to candidates consisting of object pairs without signs of additional emission, as long as the separation was not too large. This is for two reasons: first, the lensing galaxy may be too faint to detect, which is consistent with the large fraction of known doubles we miss. This fraction would undoubtedly be even higher if we chose to exclude these pairs. Second, because rather than focusing on producing the purest lensed quasar sample, we prefer to include in

our sample binary quasars and quasar pairs, which are of interest to the AGN community, for example for studies of quasar triggering (e.g., Hopkins et al. 2008), and of the small-scale quasar-quasar correlation function (e.g., Hennawi et al. 2006; Kayo & Oguri 2012).

2.2 Removal of quasar-star pairs using *Gaia*

The recent availability of the *Gaia* mission (Gaia Collaboration et al. 2016), and in particular of its second data release catalogue (DR2; Gaia Collaboration et al. 2018a), has resulted in wide application in the latest searches for lensed quasars, as demonstrated by the multitude of recent studies enumerated in Section 1. Here, we capitalize on the astrometric quantities included in this catalogue in order to further prune our list of candidates.

Gaia DR2 includes ~ 1.7 billion sources over the whole sky, with a limiting magnitude of $G \sim 21$ (Gaia Collaboration et al. 2018a). With a full width at half maximum (FWHM) of $\approx 0.1''$ (Fabricius et al. 2016), *Gaia* is effective at deblending close pairs and clusters of objects, down to $0.4''$ in DR2 (Arenou et al. 2018). Multi-epoch photometry has enabled the measurement of proper motions and parallaxes for ~ 360 million sources, and the Astrometric Excess Noise (AEN; Koposov, Belokurov, & Torrealba 2017) provides a means of separating compact galaxies from point sources. Color information ($R_p - B_p$) is also available for ~ 1.4 billion sources.

We have cross-matched our candidates with the *Gaia* DR2 catalogue, in order to identify the counterparts of both PS1 sources in each candidate (up to four sources, in case of quads). Of the 312 candidates, 307 have detections in *Gaia*, 291 of these have measured parallaxes and proper motions, and 283 have measured colors. Of their companions (i.e., the secondary component in the pair of each system, or the brightest secondary component in case of quads), the corresponding numbers are 291, 276 and 260.

We use the proper motion as a classifier, in the form of the proper motion significance defined by Lemon, Auger, & McMahon (2019), $\sqrt{(pm_{ra}/\sigma_{pm_{ra}})^2 + (pm_{dec}/\sigma_{pm_{dec}})^2}$, which includes both celestial coordinates, and where σ stands for the measured uncertainty. We adopt a limiting upper value of 5, which recovers $\sim 95\%$ of known lensed quasar images (see Figure 1 in Lemon, Auger, & McMahon (2019)). For the parallax ϖ , we use $\varpi/\sigma_\varpi \leq 4$, corresponding to a 4σ limit, since the distribution of measured parallaxes is well approximated by a Gaussian (Gaia Collaboration et al. 2018b). Finally, we use $AEN \leq 4$, corresponding to the limit which separates best between lensed quasar images and galaxies, and recovers $\sim 90\%$ of the former (see Figure 2 in Lemon, Auger, & McMahon (2019)).⁸

Our final classification of the 312 candidates is: 91 surviving candidates yet unconfirmed (1 grade A, 4 grade B and

⁸ Our chosen limits recover almost all of our confirmed candidates: amongst our 25 spectroscopically confirmed lenses or quasar pairs, only 2, both quads with 4 detected components in *Gaia*, would be (partially) ruled out based on our *Gaia* classifier: PSJ0147+4630 has one component with large parallax, and PSJ1606-2333 has one with large proper motion.

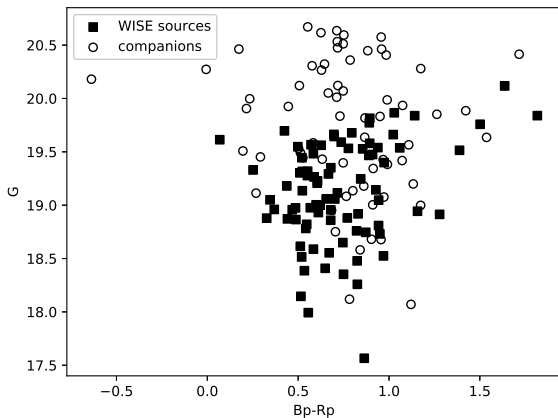


Figure 1. *Gaia* Color-magnitude plot of the main sources and companions with available colors, from the 91 surviving candidates.

86 grade C), 25 confirmed systems (6 quads, 9 doubles⁹, 10 quasar pairs), and 196 rejected candidates. We present our final sample of 91 gravitationally lensed quasar and quasar pair candidates in Table 1, together with our comments based on visual inspection and *Gaia* measurements. In Appendix B we also list the already confirmed candidates, as well as the rejected ones. From this table it can be seen that the proper motion was the dominant classifier for the overwhelming majority of candidates. Finally, Figure 1 shows that the companions have a similar distribution of *Gaia* colors with the primary sources, but are typically fainter.

2.3 Expected sample purity

In addition to the expected completeness, we also wish to estimate the purity of our sample, defined as the ratio of (number of gravitational lenses + quasar pairs)/(total number of sources in the sample). First, we perform a simple exercise where we estimate this number focusing only on the quasar pairs, and comparing the density of sources in a catalogue of point sources, and one of AGN. The idea is to estimate how many of the candidate source companions are expected to be AGN, as opposed to stars. We present the details of the computation in Appendix A. We arrive at a result of $\sim 4\%$.

The expected purity can be computed more directly using the subsample of candidates for which spectroscopic data is available in the literature. Out of 33 candidates which survive the *Gaia*-based cut and which can be either confirmed or ruled out based on the literature, 9 are doubles, 10 are quasar pairs, 6 are quads and 8 are galaxy+other, star+other or star+QSO (here “other” stands for non-QSO). For systems with $G \leq 20$ for all components (the limit at which *Gaia* is still relatively complete), these numbers are 7, 9, 5 and 5, respectively. This means that for $G \leq 20$, if we ignore the quads (there is only one quad candidate in our

final sample, and these systems are much easier to identify visually, leading to different selection), the purity for quasar pairs is $9/21 \approx 43\%$, and for doubles + quasar pairs it is $16/21 \approx 76\%$. Of course, care must be taken in interpreting this result, as the spectroscopic selection of these sources compiled from the literature is unknown.

How can the discrepant results of the two methods be reconciled? This is likely due to the known clustering of quasars, which leads to a significant enhancement of small-separation quasar-quasar pairs over expectations from uniform spatial distribution assumptions and catalogue density comparisons, and it means that the number we computed with that method must be interpreted as a lower limit. The quasar-quasar correlation function is predicted to produce an enhanced by a factor of ~ 100 on small angular scales corresponding to quasar pairs (e.g., Peng et al. 1999, and references therein). For our 91 candidates and confirmed quasar pairs we measure a median separation of $2.4''$, with a standard deviation of $0.53''$ (after removing 4 systems with separation $> 4.5''$). Kayo & Oguri (2012) do indeed estimate an increase by a factor of ~ 200 in the number of quasar pairs with separation typical for our candidates (physical scale ~ 20 kpc), over the random expectation, based on a sample of binary quasars obtained as a byproduct of a search for gravitationally lensed quasars (Oguri et al. 2006; Inada et al. 2012). This is more than enough to explain the discrepancy. In fact, multiplying this number with the fraction of AGN to point sources found in our simple exercise suggests a purity of $\sim 90\%$. This may be an overestimate, as there is a known discrepancy between the large number of predicted binary quasars (e.g., Hopkins et al. 2006) and the smaller number of discovered ones (e.g., Hennawi et al. 2010). We adopt as our best estimate of the purity the $\sim 76\%$ value measured above for quasar pairs + doubles, although we caution that this estimate might be biased due to the unknown spectroscopic selection, and applies only to $G \leq 20$. If we remove the magnitude cut, based on the spectroscopic sample, this becomes $\sim 70\%$.

In the following sections, we focus on modeling the imaging and spectroscopic data of 2M1134–2103.

3 2M1134–2103: IMAGING DATA REDUCTION AND MODELING

2M1134–2103 consists of four point-like lensed quasar images and a lensing galaxy (see Fig. 2). The lensing galaxy 2M1134–2103 can be convincingly identified in the near-infrared imaging (particularly *Ks*-band) from the VISTA Hemisphere Survey (hereafter VHS; McMahon et al. 2013, see also Fig. 2). While the relative astrometry of the quasar images, measured from VST-ATLAS (Shanks et al. 2015), is reported in L18, the VST-ATLAS data is not publicly accessible. Furthermore, the VST-ATLAS data have better seeing ($0.72''$) but the PS1 data are deeper. Therefore, we make use of archival PS1 data in our analysis. The processing of the archival PS1 data (Flewelling et al. 2016) is described in (Magnier et al. 2016a), and includes removal of the instrumental signature, image coaddition, as well as photometric and astrometric calibration (Magnier et al. 2016b). Here, we model the PS1 *grizy* and VHS *YJKs* images independently of L18.

⁹ Note that it is presently unknown whether SDSS J1320+1644, counted here as a double, is in fact a double or a quasar pair (Rusu et al. 2013).

Table 1. Sample of gravitationally lensed quasar candidates and quasar pair candidates identified systematically from PS1

Name [PS1 J...]	α	δ	#Comp	i	Sep. ["]	Rank	G mags; notes
000815-043634	2.061059	−4.609377	2	18.57	2.4	C	18.82, 20.09; similar color p-l; both componentss negligible AEN, p, pm
003309-120520	8.287252	−12.088925	3	18.10	6.8	C	18.93, 20.38; p-l (both negligible AEN, pm and p) + red inner component
004106+032726	10.273022	3.457205	2	18.43	2.4	C	18.91, 20.36; p-l; includes SDSS z=1.282 QSO;
004518+405433	11.325876	40.909217	2	18.69	3.1	C	both negligible AEN, pm and p
012221+291431	20.587958	29.242069	2	18.30	2.4	C	19.32, 18.85; similar color p-l; includes z=1.228 QSO (Huo et al. 2013);
012256+783855	20.733302	78.648546	2	18.43	2.0	C	both negligible AEN, pm and p
012648+411136	21.698143	41.193204	2	19.13	3.1	C	18.41, 20.72; similar color p-l; one component negligible AEN, pm and p;
013021+072516	22.585897	7.421231	2	18.80	2.0	C	companion has no Gaia pm and p
014114-062740	25.307825	−6.461006	2	19.05	2.4	C	18.94, 18.99; similar color p-l; both negligible AEN, pm and p
014455+271137	26.230638	27.193616	2	19.01	1.9	C	19.26, 20.15; similar color p-l; both negligible AEN, pm and p
014912+422843	27.299792	42.478624	2	17.85	2.8	C	18.98, 19.65; p-l; one component negligible AEN, pm and p;
015417+433319	28.571648	43.555321	2	18.05	2.7	C	companion has no Gaia pm and p
022205-234144	35.521817	−23.69567	2	18.99	2.1	C	20.79; similar color p-l; only one has Gaia data; negligible AEN, pm and p
022958+032031	37.492401	3.341935	2	18.02	2.1	C	19.53, 19.63; similar color p-l; both negligible AEN, pm and p
024245-100257	40.688737	−10.049076	2	18.43	2.4	C	17.99, 18.82; similar color p-l; both AEN, negligible pm and p
024950+260651	42.459532	26.114096	2	18.56	3.2	C	18.92, 18.28; similar color p-l; both negligible AEN, pm and p
042022-101932	65.092136	−10.325513	2	18.54	3.2	B	18.96, 20.45; similar color p-l; both negligible AEN, pm and p
045048-280957	72.701208	−28.165922	2	18.95	5.0	C	18.15, 18.79; similar color p-l; both negligible AEN, pm and p
051623-043755	79.096146	−4.631812	2	18.20	3.0	C	18.73, 19.50; similar color p-l; both negligible AEN, pm and p
052026-045245	80.10733	−4.879078	2	19.30	2.4	C	18.81, 20.15; similar color p-l; both negligible AEN, pm and p
052902-032948	82.260144	−3.496646	2	19.27	1.4	C	extended-p-l; no Gaia data
061215-193928	93.063509	−19.657707	2	17.49	2.2	C	18.87, 19.07; similar color p-l; both negligible AEN, pm and p
063019-264851	97.580318	−26.814116	3	18.58	3.4	C	18.48, 18.47; p-l; both negligible AEN, pm and p
064505+505755	101.269368	50.965199	2	18.84	3.0	C	19.57, 19.65; similar color p-l; both negligible AEN, pm and p
064519+380712	101.327789	38.119957	2	17.3	2.4	B	19.84, 20.37; similar color p-l; both negligible AEN, pm and p
070249+530654	105.704772	53.114994	2	19.05	2.5	C	18.26, 20.34; similar color p-l (both negligible AEN, pm and p) + red companion;
073017+152842	112.570702	15.4782	2	18.52	2.2	C	included in the Delchambre et al. (2019) Gaia clusters catalogue
081357+103304	123.486422	10.551007	2	18.62	2.7	C	19.99, 19.05, 19.54; p-l; all have negligible AEN, pm and p;
081806+524732	124.523269	52.792161	2	17.66	3.3	C	included in the Delchambre et al. (2019) Gaia clusters catalogue
085254-014850	133.223992	−1.813836	2	18.56	3.2	C	19.56, 19.14; similar color p-l; both negligible AEN, pm and p
090611-093755	136.545112	−9.632052	2	18.76	2.8	C	18.50, 17.63; similar color p-l; both negligible pm and p
091724-054200	139.348239	−5.700061	2	18.80	2.6	C	19.05, 19.65; p-l; both negligible AEN, pm and p
092823+213853	142.096969	21.647987	2	18.84	2.6	C	19.40, 18.78; similar color p-l; both negligible AEN, pm and p
094450+243459	146.208841	24.582929	2	19.08	2.4	C	18.97, 18.70; similar color p-l; includes SDSS z=0.799 QSO;
095324+570319	148.351564	57.055364	2	18.70	2.6	C	SQLS candidate; both negligible AEN, pm and p
100406+523132	151.025821	52.525602	2	19.45	2.3	C	18.96, 17.82; similar color p-l; includes SDSS z=1.793 QSO;
100809-044923	152.038129	−4.823158	2	18.56	2.9	C	SQLS candidate; both negligible AEN, pm and p
110928-233315	167.366219	−23.554197	2	19.13	2.3	C	18.51, 19.94; similar color p-l; both have negligible AEN, pm and p
111524-030727	168.850362	−3.124282	2	18.78	2.6	C	18.86, 19.66; similar color p-l; both have negligible AEN, pm and p
112145+011422	170.436445	1.239436	2	19.17	1.5	C	18.87, 19.21; similar color p-l; both have negligible AEN, pm and p
112456-230507	171.233583	−23.085325	2	19.10	1.8	C	19.05, 19.14; similar color p-l; both have negligible AEN, pm and p
113800+073004	174.495987	7.501138	2	18.25	2.8	C	19.84, 20.98; p-l; only one component has Gaia pm and p, negligible values
115458+185527	178.740065	18.924205	3	18.83	2.7	C	19.33, 18.90; similar color; includes SDSS z=0.619 QSO; SQLS candidate,
121410+333703	183.540724	33.617445	3	18.91	2.5	B	no lensing object; both have negligible AEN, pm and p
121410+292445	183.541535	29.412494	2	19.47	1.5	C	similar color p-l; no Gaia data
121710-025622	184.290272	−2.939367	2	19.08	1.7	C	18.61, 20.14; p-l; only one component has Gaia pm and p, negligible values
121756-181837	184.481806	−18.310394	2	19.42	2.5	C	19.47, 20.59; similar color; both have negligible AEN, pm and p
130451-102826	196.211716	−10.473908	2	19.00	2.2	C	20.12, 19.06; similar color p-l; both have negligible AEN, pm and p
130602+210549	196.510055	21.09696	2	18.01	2.1	C	19.35, 19.81; similar color p-l; includes SDSS z=1.292 QSO;
132202+030933	200.508342	3.159175	2	19.33	2.7	C	companion has no Gaia p and pm
135425-094103	208.60498	−9.684109	2	19.05	2.1	C	19.48, 19.51; similar color p-l; both have negligible AEN, pm and p
141855+244107	214.731082	24.685389	2	18.88	4.5	C	18.39, 19.40; similar color p-l; includes SDSS z=1.209 QSO; SQLS candidate;
142816+095443	217.065054	9.911986	2	18.63	1.8	C	no Gaia p and pm
143125-044338	217.854924	−4.727349	2	19.30	2.3	C	18.88, 20.31; similar color p-l (both have negligible AEN, pm and p) + red
143928-065828	219.867271	−6.974503	2	19.17	2.3	C	component
144446-163241	221.189796	−16.544779	2	18.59	2.0	C	19.14, 20.41; similar color p-l (one component has Gaia data, negligible AEN,
145939+162155	224.914314	16.365409	2	18.67	3.5	C	pm and p) + red component; includes SDSS z=1.774 QSO, SQLS candidate
151545+004328	228.936742	0.724443	2	18.96	3.5	C	19.81; similar color p-l; only one component has Gaia data; negligible AEN, pm
151546-032231	228.941104	−3.375202	2	19.31	2.3	C	and p
							19.68; similar color p-l; includes SDSS z=1.465 QSO (Croom et al. 2001);
							companion has no Gaia data
							19.44, 20.45; p-l; both have negligible AEN, pm and p
							19.28, 20.14; p-l; both have negligible AEN, pm and p
							third red component; no Gaia data
							19.32; similar color; includes SDSS z=0.961 QSO; SQLS candidate; companion
							has no Gaia data
							19.77; similar color p-l; only one component has Gaia data; negligible values of
							AEN, pm and p
							19.06, 20.60; similar color p-l; includes SDSS z=0.573 QSO;
							(Williams, Agnello, & Treu 2017) candidate; companion has no Gaia data
							18.55, 19.67; p-l; includes SDSS z=1.467 QSO; no lens object; both have
							negligible AEN, p and pm
							19.30, 20.10; similar color p-l; both have negligible AEN, p and pm
							19.47, 19.98; similar color p-l; both have negligible AEN, p and pm
							19.34, 18.95; similar color p-l; both have negligible AEN, p and pm
							18.88, 20.27; similar color p-l; includes SDSS z=1.569 QSO; SQLS candidate;
							both have negligible AEN, p and pm
							19.51, 19.33; similar color p-l; both have negligible AEN, p and pm
							19.53, 20.23; similar color p-l; both have negligible AEN, p and pm

Table 1 – *continued*

Name [PS1 J...]	α	δ	#Comp	i	Sep. ["]	Rank	G mags; notes
152841+393229	232.169429	39.541466	2	19.46	1.9	C	19.61, 20.35; similar color p-l; includes SDSS $z=1.215$ QSO; both have negligible AEN, p and pm
153808-192310	234.535305	-19.386104	2	19.29	2.8	C	19.54, 20.43; p-l; both have negligible AEN, p and pm
162900-140856	247.247099	-14.148889	2	18.55	2.4	C	19.76, 19.00; similar color; both have negligible AEN, p and pm
162903+372433	247.260887	37.409037	2	19.05	4.3	C	19.18, 19.40; similar color p-l; includes SDSS $z=0.926$ QSO, no lensing object; both have negligible AEN, p and pm; Williams, Agnello, & Treu (2017) candidate
164556+402246	251.482344	40.379443	2	19.01	2.3	C	19.23; similar color p-l; one component has negligible AEN, p and pm, the other has no Gaia data
165831+141605	254.627587	14.268089	2	18.73	2.2	C	19.11, 19.08; similar color p-l; both have negligible AEN, p and pm
170402+115730	256.009503	11.958322	2	18.59	2.9	C	18.75; similar color p-l; companion has no Gaia data
172406+640711	261.027058	64.119668	2	18.16	2.4	C	18.35, 20.35; similar color p-l; includes SDSS $z=1.512$ QSO; SQLS candidate; both have negligible AEN, p and pm
172751+194436	261.960528	19.743295	2	19.32	1.9	C	20.11; similar color p-l; companion has negligible AEN, p and pm; no Gaia data for main component
175526+631504	268.857193	63.251051	2	19.28	2.2	C	19.66, 19.74; similar color p-l; both components have negligible AEN, p and pm
175918+345928	269.825014	34.991208	2	19.09	2.3	C	19.21, 19.64; similar color p-l; both components have negligible AEN, p and pm
183230+534914	278.123646	53.8206	2	19.13	3.0	C	19.58, 20.15; similar color p-l; both components have negligible AEN, p and pm
184624+352002	281.599148	35.333764	2	19.33	2.4	C	19.29, 19.76; similar color p-l; both components have negligible AEN, p and pm
192808+553219	292.032689	55.538539	2	18.05	2.7	C	19.00, 18.32; similar color p-l; both components have negligible AEN, p and pm
195243-111715	298.179179	-11.28742	2	19.46	2.3	C	19.70, 20.32; similar color p-l; both components have negligible AEN, p and pm
204258-273754	310.739743	-27.631602	2	19.15	2.3	C	19.14, 20.47; similar color p-l; both components have negligible AEN, p and pm
205006-225929	312.523434	-22.991253	2	18.93	2.3	C	19.00, 20.22; similar color p-l; both components have negligible AEN, p and pm
205143-111444	312.931008	-11.245566	3	18.95	3.2	A	19.66, 19.93, 20.74; p-l sources in quad-like configuration. 2 components have negligible AEN, p and pm, another has negligible AEN and no other Gaia data; the final one has no Gaia data ^a
212028+280324	320.116547	28.056796	2	18.65	2.9	C	18.78, 19.41; similar color p-l; both components have negligible AEN, p and pm
213736+201517	324.398524	20.254669	2	19.29	1.6	C	19.64, 19.66; similar color p-l; both components have negligible AEN, p and pm
214132+182621	325.382786	18.439197	2	18.97	2.4	C	18.96, 19.65; similar color p-l; both components have negligible AEN, p and pm
214237+255423	325.654002	25.906285	2	18.81	2.9	B	18.76; similar color p-l; only one component has Gaia data, negligible AEN, p and pm
214315+075120	325.810482	7.855534	2	18.18	2.7	C	18.52, 19.00; similar color p-l; both components have negligible AEN, p and pm
215034-265214	327.643528	-26.870639	2	16.95	1.8	C	includes $z=0.115$ (lensing?) galaxy (Jones et al. 2009); no Gaia data
215158+111102	327.99043	11.183861	2	18.77	2.6	C	19.06, 19.74; similar color p-l; includes SDSS $z=1.797$ QSO; SQLS candidate; both have negligible AEN, p and pm
220943+043217	332.428196	4.538084	2	18.18	2.9	C	18.59, 18.40; similar color p-l; both have negligible AEN, p and pm
222108+214518	335.283056	21.754907	2	17.34	3.5	C	17.57; different color p-l; only the main component has Gaia data, negligible AEN, p and pm
230339+345343	345.91142	34.89518	3	18.36	7.1	C	18.65, 18.98; similar color p-l (both have negligible AEN, p and pm) + inner red source
231813+025028	349.554123	2.841082	2	19.31	3.2	C	19.59, 19.43; similar color p-l; both have negligible AEN, p and pm
232223+375439	350.595174	37.910703	2	19.23	2.2	C	19.87, 20.81; p-l; both have negligible AEN, p and pm
232449-122555	351.205773	-12.432025	2	18.93	1.8	C	19.25; p-l; only one component has Gaia data, negligible AEN, p and pm
233525+184309	353.85286	18.71912	2	19.31	1.9	C	red components; no Gaia data

Here α and δ are the right ascension and declination of the candidates in the International Celestial Reference System. “#Comp” refers to the number of components, where we use the number of PS1 sources inside $3''$ radius, but revise it based on visual inspection, removing spurious sources and counting additional objects which appear to be part of the system. The measured separation (“Sep.”, in arcseconds) is that between the lens candidate point sources or, in case of a quad, the maximum separation between any of the point sources, taken from the PS1 catalogue, or revised as described above. The magnitude is given in i -band in the AB system for the brightest resolved component. We quote the `iMeanPSFMag` measurements from the PS1 catalogue, or the `SExtractor` (Bertin & Arnouts 1996) `MAG_AUTO` in case we had to manually add the brightest component of the system, as described above. We also quote the *Gaia* G -band magnitudes for each system, in the order of increasing separation from the WISE source coordinates. Here “p-l” stands for “point-like”, whereas “AEN” (astrometric excess noise), “p” (parallax) and “pm” (proper motion) are *Gaia*-based measurements. We list in this table the alphabetic ranking as gravitationally lensed quasars for all systems with an average grade of 1 and above, based on three human graders, as detailed in Section 2. We follow the following convention for the alphabetic ranking: A: average grade > 2.5 ; B: average grade > 1.5 ; C: average grade ≥ 1 . SQLS refers to the SDSS Quasar Lens Search (Inada et al. 2008, 2010, 2012). SDSS spectra were searched inside Data Release 14 (Abolfathi et al. 2018).

^a After the first draft of this work (arXiv:1803.07175v1), this system was independently announced by Delchambre et al. (2019) as a candidate. Our `Glaic` modeling of the observed configuration with a $SIE+\gamma$ mass profile results in a perfect fit, but the model is under-constrained because the lensing galaxy is not detected.

For our detailed modeling of 2M1134–2103 we downloaded from the PS1 and VHS archives $180'' \times 180''$ cutouts around the system in all available filters, large enough to contain stars to model the PSF and to improve the image orientation. We subtracted the sky background from the VHS images using `SExtractor` (Bertin & Arnouts 1996), and re-sampled all images with `Swarp` (Bertin et al. 2002) to a common orientation. We measured final pixel scales with `Scamp` (Bertin 2006).

We model the system with `hostlens` (Rusu et al. 2016). `Hostlens` models an arbitrary number of point-like and

extended sources using a common point-spread function (PSF), either specified by the user from nearby stars, or fitted to the data as a sum of two concentric Moffat (Moffat 1969) profiles. We find that modeling the quasar images using nearby stars as PSFs results in significant residuals, which could affect the image flux measurements and the characterization of the lensing galaxy. We therefore model the data using an analytical PSF fitted to the data. To remove residuals still remaining at the centers of the three bright quasar images in the *rizYJKs* bands, we use the PSF reconstruction technique described in Chen et al. (2016),

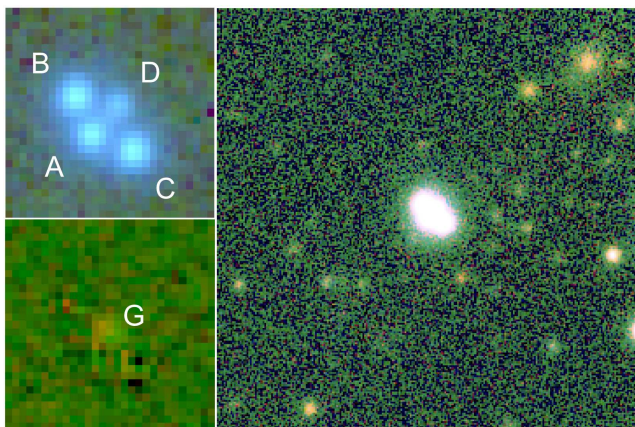


Figure 2. *Upper left:* Color composite (VHS-YJKs) of 2M1134–2103 showing the four lensed quasar images (A, B, C and D). Image is $10''$ on the side. *Lower left:* The same color composite, after subtracting the four quasar images with `hostlens`, shows the presence of a lensing galaxy G. *Right:* Color composite (riz) using PS1 data shows the immediate environment of the lens system, which is located at the center. Image is $60''$ on the side. All images are oriented such that North is up and East is to the left.

with the best-fit analytical PSF as a starting point. This technique reconstructs the PSF iteratively, on a grid of pixels, under the assumption that the PSF does not vary across the quasar images. The remaining residuals at the location of the quasar images are small, as can be seen in Fig. 3.

In the PS1 data we do not detect any sign of the lensing galaxy, which however stands out in the VHS *J* and *Ks* images. We model its light profile in these bands simultaneously with the quasar images, using a de Vaucouleurs (de Vaucouleurs 1948) profile commonly used for early-type lensing galaxies. A circular profile fits the emission from the lensing galaxy well, without leaving noticeable residuals. Using a Markov Chain Monte Carlo (MCMC) approach, we find that the lensing galaxy flux is highly degenerate with the effective radius of the de Vaucouleurs profile, and is therefore unreliable.

In order to perform gravitational lens modeling of 2M1134–2103 we need to estimate reliable relative astrometry for the quasar images and the lensing galaxy. For the three brightest quasar images we take the mean and scatter between the measured relative astrometry in different filters (excluding *g*-band, where the seeing is significantly larger, see Table 2), whereas for the lensing galaxy and the faint counter-image D, we only use the *J* and *Ks* filters. Indeed, the separation between the brighter images (A, B and C) and the fainter counter-image (D) decreases slightly with increasing wavelength in the PS1 images, because of the progressively increasing flux contribution from the red lensing galaxy. We report our measured astrometry and photometry in Table 2. Our astrometry is consistent with the one presented in L18 within our 2σ uncertainties.

4 2M1134–2103: KECK SPECTROSCOPY

The 2M1134–2103 lens system was observed with the Echellette Spectrograph and Imager (ESI; Sheinis et al.

2002) on the night of 2017 Nov 18 UT (program number 2017B_U110). The observations utilized a slit with a width of $1''$ and the cross-dispersed echellette mode of the spectrograph, which provides a constant dispersion of roughly $11.5 \text{ km sec}^{-1} \text{ pix}^{-1}$ over a wavelength range of approximately 3900 to 11000 Å. Here, we follow the nomenclature of L18. Two slit position angles were used, one oriented at $+46.7^\circ$ (N through E) in order to go across lensed images B and C (henceforth the “BC slit”) and one oriented at -42.3° to cover images A and D (the “AD slit”). We obtained three 600 s exposures through the BC slit and four 600 s exposures through the AD slit.

We calibrated the data using a custom pipeline written in Python. The pipeline does a flat-field correction, rectifies the two dimensional spectra, does the wavelength calibration using both arc lamp and night sky emission lines, and subtracts the sky emission. The calibrated data for both slits are shown in Fig. 4. In the AD slit, the two-dimensional spectra show one bright trace that is heavily blended with a much fainter trace, while the BC slit shows three clearly separated traces. We identify the three traces in the BC slit with components B, A+D+G, and C in the imaging data. Based on the imaging, we expect that the emission from image A completely dominates the central trace.

We extracted one-dimensional spectra from the exposures on both slits using a second Python pipeline that extracts the spectra from each spectral order, applies a response correction based on observations of a spectrophotometric standard, in this case Feige 110, and finally combines the data from each of the 10 spectral orders into one final spectrum. For the AD slit, we only extracted one aperture that we identify with a blend of A, D, and G, while for the BC slit we extracted separate apertures corresponding to B, A+D+G, and C. Note that the AD slit may very well contain significant scattered light from images B and C. The extracted spectra are shown in Fig. 5 and all show clear broad emission lines that, furthermore, are indicative of quasars at a redshift of $z_{\text{src}} \sim 2.77$. Thus, the ESI spectra are fully consistent with the interpretation of 2M1134–2103 as a quad lensed quasar. An exact value of the source redshift is difficult to obtain due to the fact that the peaks of the lines used for redshift determination are affected by absorption systems (Fig. 5; also e.g., Lee 2018). The measured redshift is smaller than the $z \sim 3.5$ estimate in L18, based on PS1 colors.

In addition to the broad emission lines, all of the spectra show a number of absorption lines. In the range 5000–7500 Å, these correspond to absorption features of Fe and Mg, and are consistent with two separate absorption systems at $z_{\text{abs},1} = 1.554$ and $z_{\text{abs},2} = 1.481$. The first system has stronger lines in the A+D+G and B spectra, while the second is stronger in the image C spectrum. Although it is possible that these systems may be associated with the primary lensing galaxy, the narrowness of the lines makes this interpretation unlikely. A much stronger indication of the lensing galaxy would be the detection of stellar absorption lines, such as the CaII H and K lines, with widths consistent with the velocity dispersions of $>100 \text{ km s}^{-1}$ expected for a massive lensing galaxy. If these corresponded to the redshifts of the absorption features mentioned above, they would be observed at wavelengths longer than the ones plotted in Fig. 5, where we have extracted robust spectra.

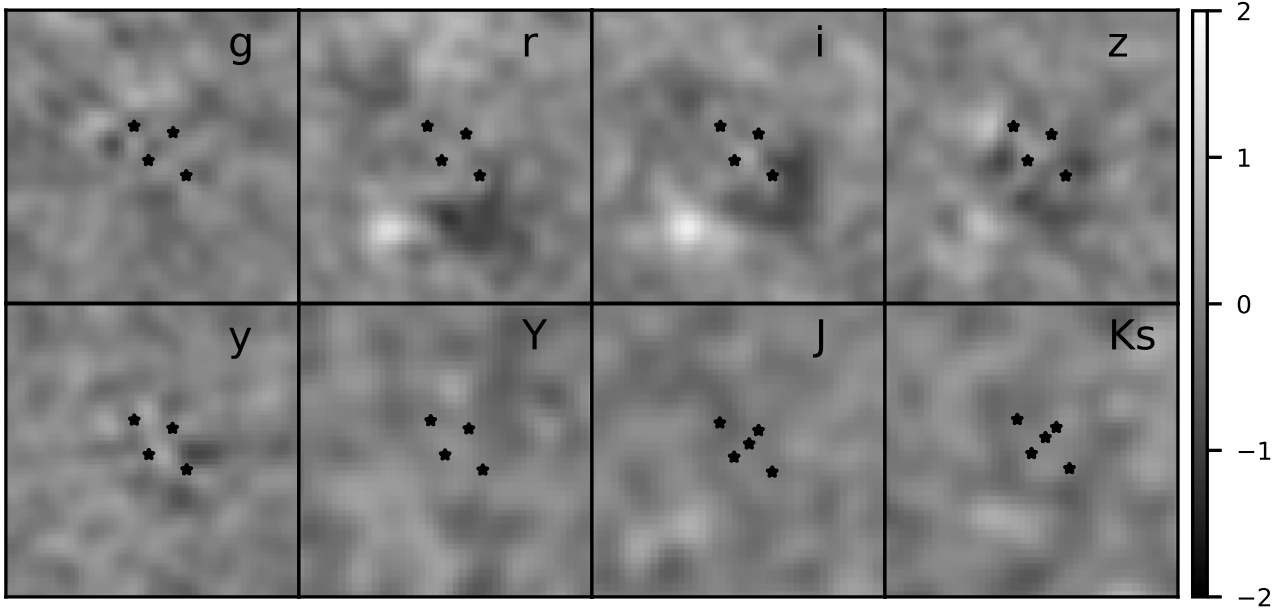


Figure 3. Residuals after morphological modeling of imaging data with *hostlens*. The size of the cutouts is $15'' \times 15''$. The images were divided by the associated noise maps, then smoothed with a 3-pixel Gaussian, to enhance structure. The positions of the components that were modeled in each band (A, B, C, D, as well as G in *JKs*) are marked with star symbols. Object GX to the south-east of the lens, conspicuous in the *r* and *i* bands, is left unmodeled (see Section 5) .

Table 2. Relative astrometry and absolute photometry of 2M1134–2103

Filter (lim. mag)	A	B	C	D	G	GX	Seeing ["]
all (x-axis)	0.000 ± 0.000	-0.733 ± 0.005	1.944 ± 0.006	1.262 ± 0.014	0.74 ± 0.04	-2.50 ± 0.05	
all (y-axis)	0.000 ± 0.000	1.757 ± 0.006	-0.776 ± 0.006	1.350 ± 0.020	0.75 ± 0.10	-3.32 ± 0.05	
<i>g</i> (24.2)	17.08 ± 0.005	17.37 ± 0.005	17.26 ± 0.005	18.90 ± 0.014	–	–	1.70
<i>r</i> (24.5)	16.85 ± 0.005	17.06 ± 0.005	17.00 ± 0.005	18.67 ± 0.005	–	$[23.37 \pm 0.10]$	1.20
<i>i</i> (24.5)	16.81 ± 0.005	16.88 ± 0.005	16.83 ± 0.005	18.46 ± 0.005	–	$[21.75 \pm 0.08]$	1.20
<i>z</i> (23.6)	16.87 ± 0.005	16.90 ± 0.005	16.87 ± 0.005	18.49 ± 0.006	–	–	1.10
<i>y</i> (22.6)	16.79 ± 0.04	16.72 ± 0.03	16.70 ± 0.03	18.29 ± 0.04	–	–	1.00
<i>Y</i> (22.2)	16.08 ± 0.008	15.98 ± 0.007	16.02 ± 0.007	17.57 ± 0.016	–	–	0.85
<i>J</i> (21.4)	15.92 ± 0.005	15.81 ± 0.005	15.83 ± 0.005	17.35 ± 0.012	$[19.05 \pm 0.12]$	–	0.85
<i>Ks</i> (20.1)	15.34 ± 0.006	15.13 ± 0.006	15.19 ± 0.009	16.81 ± 0.027	$[17.33 \pm 0.09]$	–	0.85

Relative astrometry is determined by using information from multiple filters (See Section 3). The units are arcseconds and the sign convention is positive from E to W (x-axis) and from S to N (y-axis). The ICRS position of image A in the PS1 catalogue is (J2000.0) 11:34:40.588 –21:03:23.06. Magnitudes are in the AB (*grizy*) and Vega (*YJKs*) systems, and are corrected for Galactic extinction following Schlafly & Finkbeiner (2011). The 1σ limiting magnitudes are computed in $2''$ -radius blank sky apertures around the system. The errors on magnitudes are those from MCMC, with the minimum uncertainty boosted to 0.005 mag, and do not include zeropoint or PSF uncertainties. The magnitudes of G and GX (see Section 5) should be considered unreliable, as in order for the fit to converge, the effective radius was fixed to < 1 pixel.

5 2M1134–2103: GRAVITATIONAL LENS MODELING

We perform gravitational lens mass modeling of 2M1134–2103 with *glafic* (Oguri 2010), using the observed relative positions of the quasar images and the lensing galaxy as constraints. We do not impose constraints based on the flux ratios, as these might be affected by microlensing, extinction, and intrinsic variability (e.g., Yonehara, Hirashita, & Richter 2008). However, we analyze

the observed flux ratios under the assumptions that they are dominated by extinction, in Section 5.1.

We start with the same mass model used in L18, a singular isothermal sphere with external shear (SIS+ γ). This model has $\chi^2/\text{d.o.f.} = 7.5/3$ (where d.o.f. stands for degrees of freedom), most of which is due to the difference between the measured and predicted position of image D relative to the lens G. We recover the results of L18, in particular that an unusually large shear of ~ 0.34 at 44 deg W of N is required to fit this system.

Secondly, we fit a model which allows for mass elliptic-

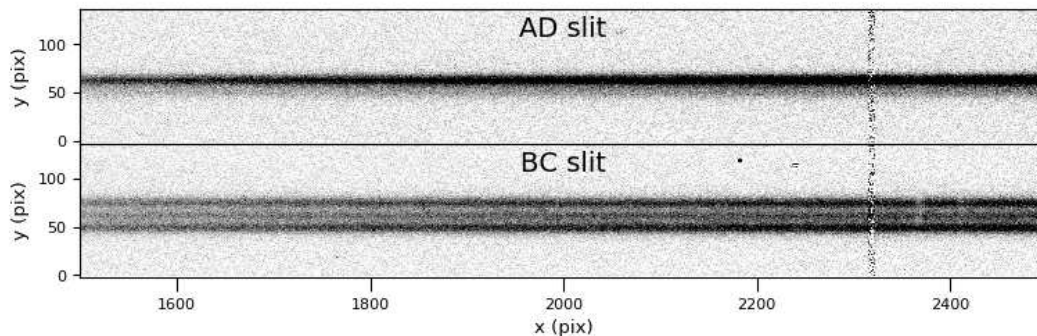


Figure 4. Examples of the calibrated and sky-subtracted spectra obtained with Keck/ESI of 2M1134–2103. Data are from the AD slit (top) and the BC slit (bottom), with spectra showing a portion of the fifth of ten spectral orders recorded by the spectrograph.

ity, SIE+ γ . Indeed, quads have enough constraints to disentangle internal and external sources of shear, and our fit shows a dramatic improvement to $\chi^2/\text{d.o.f.} = 0.1/1$. This model requires a shear of ~ 0.39 , slightly larger than before, and a mass axis ratio of $0.80^{+0.10}_{-0.18}$, with the long axis at 37^{+5}_{-13} deg E of N, almost perpendicular to that of the shear. While our imaging data does not have sufficient resolution to fit an elliptical light profile to the lensing galaxy, studies of quads show that the mass and light profiles of lensing galaxies are typically aligned (e.g., Keeton, Kochanek, & Falco 1998; Sluse et al. 2012). We note that Rusu & Lemon (2018) modeled a different quad, GraL J1817+2729, in a cross-like configuration, and showed that while an SIE+ γ model required large shear and large ellipticity, with the long axis perpendicular to the shear, similar to the present case, a Sersic+SIS+ γ model, where the Sersic component stands for the baryonic matter in the disk of the lensing galaxy, significantly diminishes the required shear, and changes its orientation. We attempted to fit such a model here, but it behaves equivalently to our SIE+ γ model, requiring similar orientation and large shear. It appears that the highly stretched, diamond-like configuration, cannot be explained by internal sources of shear.

As both the SIS+ γ and SIE+ γ models are consistent in their requirement of large external shear, we look for potential sources of shear from the surrounding environment. In Fig. 2 we display a $60'' \times 60''$ color composite image around 2M1134–2103, which clearly shows a group of red galaxies in the upper right corner, the brightest of which is a $i = 19.32$ galaxy located at $\alpha = 173.6620$, $\delta = -21.0502$, $30''$ from the quad, in the direction of 45 deg W of N. The PS1 and VHS colors of this galaxy imply a photometric redshift of 0.70 ± 0.09 , estimated with BPZ (Benítez 2000). The existence of the galaxy group at this location implies that it is responsible for part of the measured shear. However this is unlikely to be the complete picture, as an SIS profile at the location of this galaxy would require a very large velocity dispersion $\gtrsim 1100$ km/s to produce the measured shear, depending on the redshift of the lensing galaxy in 2M1134–2103.

Fig. 3 reveals another clue, closer to 2M1134–2103. After subtracting the quasar images, an additional component is detected in filters r and i , $4.16''$ from image A, also in the direction of the shear, towards south-east. It is unclear whether this new component, which we name GX, is a galaxy or a star, as it is too faint ($i \sim 21.75$) to constrain its mor-

phology. Under the assumption that it is a galaxy, its colors suggest a redshift lower than the one of the lensing galaxy, which is only detected in the near-infrared VHS filters. We incorporate GX into a third lensing model, in order to estimate its effect on the external shear. As we do not know the redshifts for either G or GX, we consider the simplest case in which G and GX are modeled as SIS of equal strength, at the same redshift. This model is expected to be an upper limit to the contribution of GX to the lensing configuration, as GX is likely a lower redshift, low mass galaxy. We obtain a good fit with $\chi^2/\text{d.o.f.} = 2.3/3$, and a residual external shear of ~ 0.19 , oriented as before. In this model, the two lenses are located ~ 4 Einstein radii apart, in units of the Einstein radius of G. Our model shows that GX can explain a significant fraction of the shear we measured in our initial SIS+ γ model. We expect that in reality most of the measured shear is an interplay between the effects of GX and the nearby group. In our model incorporating GX, the nearby group would still require a velocity dispersion of ~ 800 km/s to account for the remaining shear, which would imply $\gtrsim 50$ group/cluster members (e.g., Berlind et al. 2006). While we do not see more than ~ 3 possible galaxy members in the PS1 image, this is not an argument against the existence of this structure, as the PS1 images are shallow. Indeed, PS1 images of the system RX J0911+05 reveal only ~ 5 galaxies part of a spectroscopically confirmed cluster with at least 24 members at a similar redshift of $z = 0.769$, with velocity dispersion ~ 800 km/s (Kneib, Cohen, & Hjorth 2000), giving rise to a very large shear $\gtrsim 0.3$ (Sluse et al. 2012).

We note that another lensed system with a remarkably similar diamond-like configuration has recently been discovered (Bettoni et al. 2019) close to a galaxy cluster, also with a large measured shear of 0.31 and a nearby galaxy in the direction of the shear. Finally, we note that highly-sheared quadruple lens systems are not unexpected, and are a consequence of the tendency of elliptical galaxies, which constitute most of the lensing galaxies, to reside in overdense regions with high shear (e.g., Holder & Schechter 2003). We conclude that the large shear values we measure do not, therefore, point out to a problem with our mass models.

In the analysis above we did not assume particular values of source and lens redshifts, except when we estimated the velocity dispersion of the galaxy group at $z \sim 0.7$. The flux ratios are also insensitive to the choice of redshifts, however the estimated time delays depend on them. To estimate

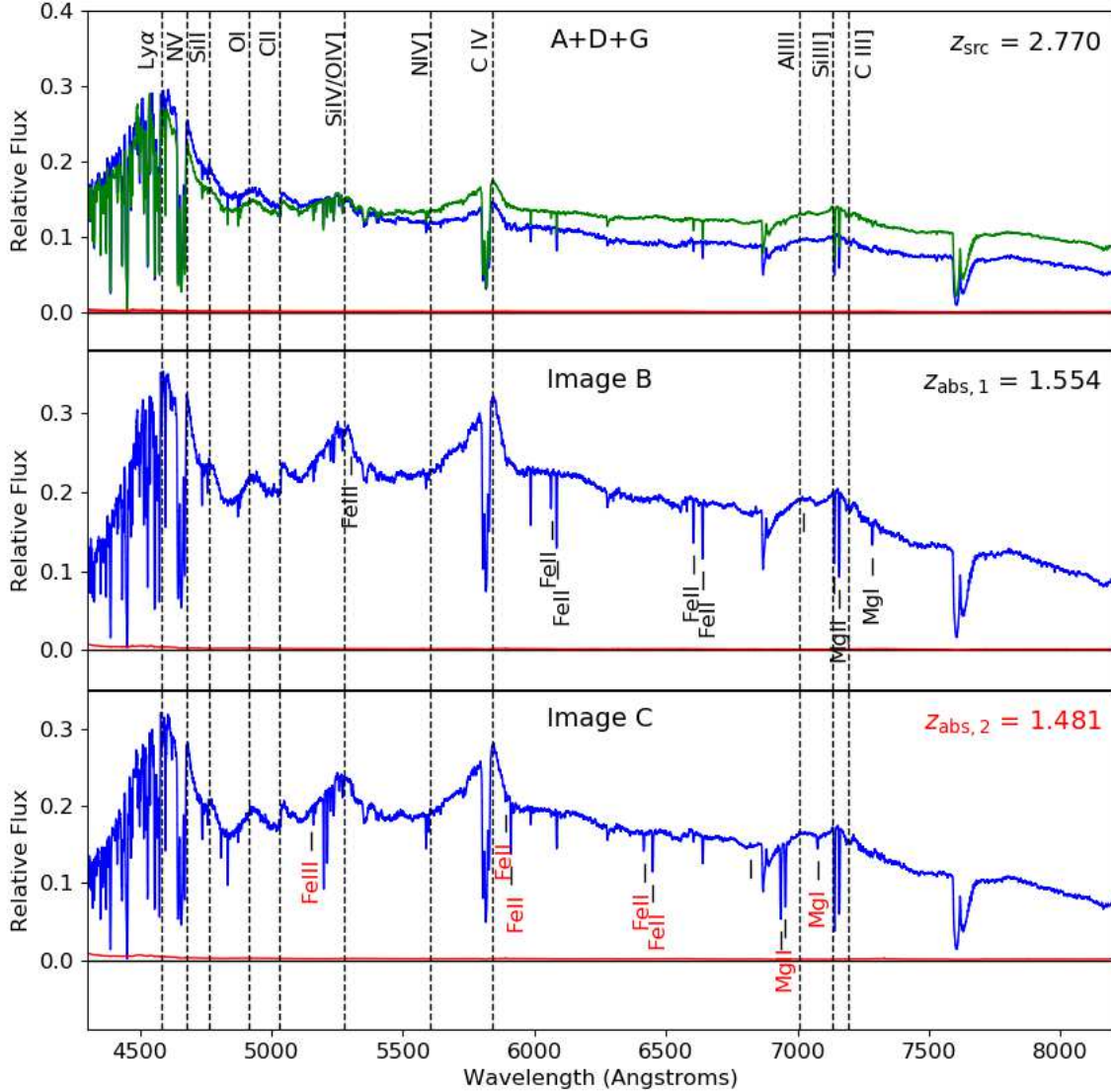


Figure 5. ESI spectra of 2M1134–2103. Combined light from lensed images A and D, plus any emission from the lensing galaxy is visible in the spectrum extracted from the AD slit (green) as well as that from the BC slit (dark blue) in the top panel. Spectra of images B (middle) and C (bottom) are extracted from the BC slit. The rms noise of each spectrum is plotted in red. Identified emission and absorption systems are labelled (see further explanation in Section 4). The wide absorption doublet at ~ 7650 Å is telluric. The spectra were smoothed using a 3-pixel boxcar with inverse-variance weighting.

the time delays, which are of interest to cosmography studies (e.g. Bonvin et al. 2017), we use the source quasar redshift $z_s = 2.77$ measured from spectroscopy, and the lens redshift limits we infer below in Section 5.1, $z_l \sim 0.45 - 1.5$. For $z_l \sim 0.45$ and the SIS+ γ model, the estimated time delays are $\Delta CB \sim 7$ days, $\Delta CA \sim 30$ days and $\Delta CD \sim 55$ days. The order of the image time arrival is the same in all three models, with image C leading. We summarize the main pa-

rameters of the mass models we employed in Table 3, along with the corresponding time delays.

5.1 Flux ratio analysis and the lens redshift

We show the measured image flux ratios in Fig. 6, based on Table 2. At least three of the six ratios show a clear dependence on wavelength. Interpreted as due to extinction, these ratios imply that A is the least reddened image, in agree-

Table 3. Summary of the best-fit parameter values of the lensing mass models, and the predicted time delays

Model	z	σ [km/s]	e	θ_e	γ	θ_γ	ΔCA	ΔCB	ΔCD
SIS+ γ	0.45	243.0	—	—	0.34	43.6	30.5	6.8	54.8
SIS+ γ	1.50	384.1	—	—	0.34	43.6	196.6	43.9	353.1
SIE+ γ	0.45	242.1	0.33	−39.9	0.39	45.2	24.7	6.3	43.6
SIE+ γ	1.50	382.6	0.33	−39.9	0.39	45.2	159.0	40.3	281.0
2SIS+ γ	0.45	233.3	—	—	0.19	45.8	33.9	7.5	44.3
2SIS+ γ	1.50	363.4	—	—	0.19	45.8	225.9	49.3	263.4

Here z is the lens redshift, σ is the lens velocity dispersion, e and γ are the lens ellipticity and shear, respectively, and θ_e and θ_γ are their orientations (W of N). The time delays (last column) are in units of days.

ment with image D being closest to the lensing galaxy, and the major axis of the lensing galaxy being oriented towards B and C (with B more reddened than C), according to the SIE+ γ model. We also show in Fig. 6 the predicted flux ratios given by the SIS+ γ model. The predicted SIE+ γ fluxes are very similar, within $\sim 10\%$, but the G+GX+ γ model predicts a demagnified image A, about as bright as D. All models predict image B to be the brightest, as observed in the VHS data. The predicted B/C is invariant across all three models, as the shear is almost perpendicular to the direction of these two images. In fact, this ratio is the only one which matches the observations, in the reddest filter.

Flux ratios of quasar images have been used in the past to study the extinction properties of lensing galaxies (e.g., Falco et al. 1999) as well as to infer lens redshifts (e.g., Jean & Surdej 1998). Here, we use them to infer the lens redshift z_l as well as the de-reddened flux ratios (relative magnifications) M_i , where i refers to each of the six image pairs, independent of the chosen mass model. Following Falco et al. (1999), we optimize these parameters as well as the differential extinctions E_i and the shape of the extinction curve R by minimizing

$$\chi^2 = \sum_{j=1}^{N_\lambda} \sum_{i=1}^{N_{\text{imag}}} \frac{\left[m_i^r(\lambda_j) - m_i^b(\lambda_j) - 2.5 \log M_i - E_i R \left(\frac{\lambda_j}{1+z_l} \right) \right]^2}{\sigma_{ij}^{b,2} + \sigma_{ij}^{r,2}} \quad (1)$$

where j is the filter index, superscripts b and r refer to the blue and red images in each pair, respectively, and σ_{ij} is the magnitude measurement uncertainty. We use the central wavelength of each filter, and the Cardelli, Clayton, & Mathis (1989) extinction function implemented in the code `extinction`¹⁰. We perform the minimization using the Nelder-Mead (Nelder & Mead 1965) method implemented in `Scipy` (Oliphant 2007), starting from random positions in the parameter space and further exploring around the solution with `emcee` (Foreman-Mackey et al. 2013), to ensure that we have found the global solution.

We find the best-fit solution ($\chi^2/\text{d.o.f.} = 213.4/16$)¹¹

¹⁰ <http://extinction.readthedocs.io/en/latest/>

¹¹ With four images, thus three independent flux ratios in each band, and with eight bands, we have 24 constraints. As parameters, we have the redshift, the extinction curve parameter, three independent extinctions and 3 independent magnifications, thus eight parameters, resulting in 16 degrees of freedom.

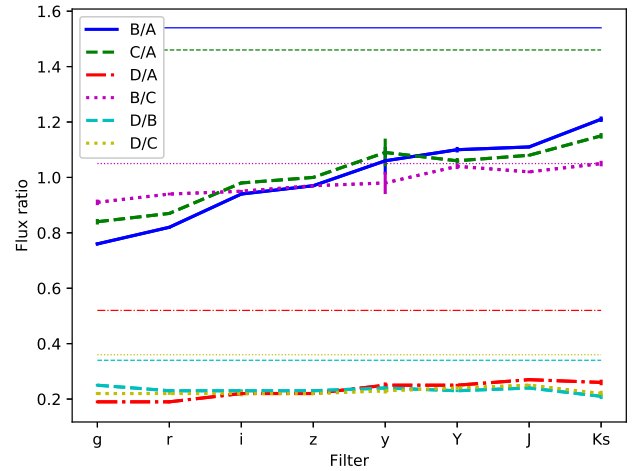


Figure 6. Measured and model-predicted flux ratios of the four quasar images. Thick lines connect observed flux ratios in all available filters, and thin horizontal lines of corresponding colors mark the flux ratios predicted by the SIS+ γ lens mass model.

with $z_l \sim 0.45$, $R \sim 2.5$ slightly smaller than the Galactic extinction curve with $R_V = 3.1$, small $E_i \lesssim 0.1$ consistent with the results in Falco et al. (1999), and flux ratios $B/A = 1.28$, $C/A = 1.20$, $D/A = 0.30$. These parameter values are robust if we remove from the fit all image pairs containing D (new fit $\chi^2/\text{d.o.f.} = 145.8/10$), in case our decomposition of G and D is problematic due to the low image resolution. They are also robust to the choice of the extinction function. Except for B/C, which matches the prediction of the mass models, the flux ratios are smaller than predicted. The quality of the fits is statistically poor, although such large χ^2 values are found by e.g., Falco et al. (1999) in other lensing systems as well. In our analysis, we have ignored any contribution from microlensing and quasar intrinsic variability, which can also affect flux ratios chromatically (e.g., Yonehara, Hirashita, & Richter 2008).

We can look for signs of microlensing by plotting the quasar image spectral ratios. While the overall shape of these ratios is sensitive to observational effects such as sub-optimal slit placement and differential refraction, these (as well as differential extinction) should affect both continua and emission lines equally. On the other hand, microlensing is dependent on the size of the source, such that the continuum emission, which originates from a more compact region than the broad emission lines, should be preferentially microlensed. Fig. 7 clearly shows that, when dividing

the fluxes of B and C to those of A_{BC} (i.e. the A+D+G signal, dominated by A, and extracted from the BC slit) and of A_{AD} , there is a large jump in the flux ratios at the locations of the SiV/OIV ($\sim 5270\text{\AA}$) and CIV ($\sim 5800\text{\AA}$) broad line regions, compared to the surrounding continuum. On the other hand, B/C is relatively flat over the entire plotted range, which means that microlensing affects image A+D (the saddle points of the time arrival surface) but not B and C. A direct comparison of the photometric flux ratios in Fig. 6 with the spectroscopic ratios in Fig. 7 is not possible due to the fact that the spectra are affected by slit losses. Indeed, this can be seen from the monotonic variation in A_{AD}/A_{BC} , which we attribute to the fact that ESI does not use an atmospheric dispersion corrector, thus resulting in flux losses from differential refraction, particularly between the orthogonally placed AD and BC slits. Also, the datasets are not concurrent, and are therefore prone to time-varying microlensing and intrinsic variability effects.

As discussed above, microlensing in particular may affect the inferred lens redshift. We note that due to the low image resolution, proximity to image D, and morphological compactness which may affect the extracted photometry, we could not obtain a robust photometric redshift for this galaxy. Looser but more robust redshift constraints can be set by using the observed image separation and the estimated magnitude of the lens in the filter in which it is brightest. On the one hand, the image separation gives the lens velocity dispersion as a function of redshift; on the other, assuming an early-type spectral template, the measured magnitude can be converted into a rest-frame absolute magnitude as a function of redshift¹², and then into a velocity dispersion (Faber & Jackson 1976). We find a lower limit of $z_l \sim 0.5$, below which the two velocity dispersion estimates disagree, and an upper limit of $z_l \sim 1.5$, above which the lens velocity dispersion is ~ 400 km/s, a value above which the galaxy velocity dispersion function is vanishingly small (Sheth et al. 2003). The lower limit is close to the value inferred from our flux ratio analysis, and the upper one is consistent with the redshift of the narrow absorption systems identified in Section 4; it is also above the L18 estimate of $z_l \sim 1$.

6 CONCLUSIONS AND FUTURE WORK

We have carried out a systematic search for gravitationally lensed quasars in PS1, based on visual examination of cutouts around the AGN source catalogue of Secrest et al. (2015), and aided by astrometric quantities measured by *Gaia*. We present our sample of 91 promising candidates, not found in the available literature, in Table 1, in order to enable follow-up observations by the interested community. We expect that the main source of contaminants are quasar pairs, which we see as a byproduct of our work, and to a lesser extent, quasar + star pairs. Our best estimate of the purity of our sample, in terms of lensed doubles and quasar pairs contaminated by quasar + star pairs, is $\sim 70\%$.

As part of our search, we have independently discovered

six known quads, including 2M1134–2103. We present, for the first time, spectroscopy of this system, confirming it as a lensed quasar with source redshift $z \sim 2.77$. We identify absorption systems at $z \sim 1.5$, in three of the resolved quasar images, but we find these to be too narrow to attribute to the lensing galaxy. The image flux ratios show a monotonic dependence on wavelength, which we use to obtain a rough estimate of the lens redshift, under the assumption that the dependence is caused by extinction. The spectral flux ratios show evidence of microlensing in the combined emission from images A and D.

Our mass modeling confirms that 2M1134–2103 is affected by large shear, for which we identify two potential sources: a group of galaxies at $z \sim 0.7$, $30''$ from the lens, and another faint companion $\sim 4''$ away. Future multi-object spectroscopy is required to determine whether these are part of a larger cluster, or physically associated with the lens. The large image separation, brightness and estimated time delays ranging from several days to several months, depending on the lens redshift, make this a valuable system to use for cosmography (e.g., Bonvin et al. 2017), provided that the environment can be characterized with future, deep imaging and spectroscopy (e.g., Sluse et al. 2017; Rusu et al. 2017; Wilson et al. 2016). High resolution *Hubble Space Telescope* or adaptive optics imaging is necessary to constrain the morphology of the lensing galaxy, and to further constrain the mass models using the expected extended emission from the underlying host galaxy (e.g., Chen et al. 2016; Wong et al. 2017).

ACKNOWLEDGEMENTS

The authors are indebted to the anonymous referee for thoroughly checking the sample of candidates, resulting in a significant improvement of our selection, and for suggesting the use of *Gaia*. We also wish to thank Paul L. Schechter for his “matchmaking” which has made this paper possible. This research made use of *Astropy*, a community-developed core Python package for Astronomy (Astropy Collaboration et al. 2013). Plots were produced with *Matplotlib* (Hunter 2007). This work was supported by World Premier International Research Center Initiative (WPI Initiative), MEXT, Japan. C.D.F. acknowledges support from the National Science Foundation under Grant No. AST-1715611.

The Pan-STARRS1 Surveys (PS1) and the PS1 public science archive have been made possible through contributions by the Institute for Astronomy, the University of Hawaii, the Pan-STARRS Project Office, the Max-Planck Society and its participating institutes, the Max Planck Institute for Astronomy, Heidelberg and the Max Planck Institute for Extraterrestrial Physics, Garching, The Johns Hopkins University, Durham University, the University of Edinburgh, the Queen’s University Belfast, the Harvard-Smithsonian Center for Astrophysics, the Las Cumbres Observatory Global Telescope Network Incorporated, the National Central University of Taiwan, the Space Telescope Science Institute, the National Aeronautics and Space Administration under Grant No. NNX08AR22G issued through the Planetary Science Division of the NASA Science Mission Directorate, the National Science Foundation Grant No.

¹² We use the `mag2mag` routine from Auger et al. (2009), available at <https://github.com/tcollett/LensPop/tree/master/stellarpop/>

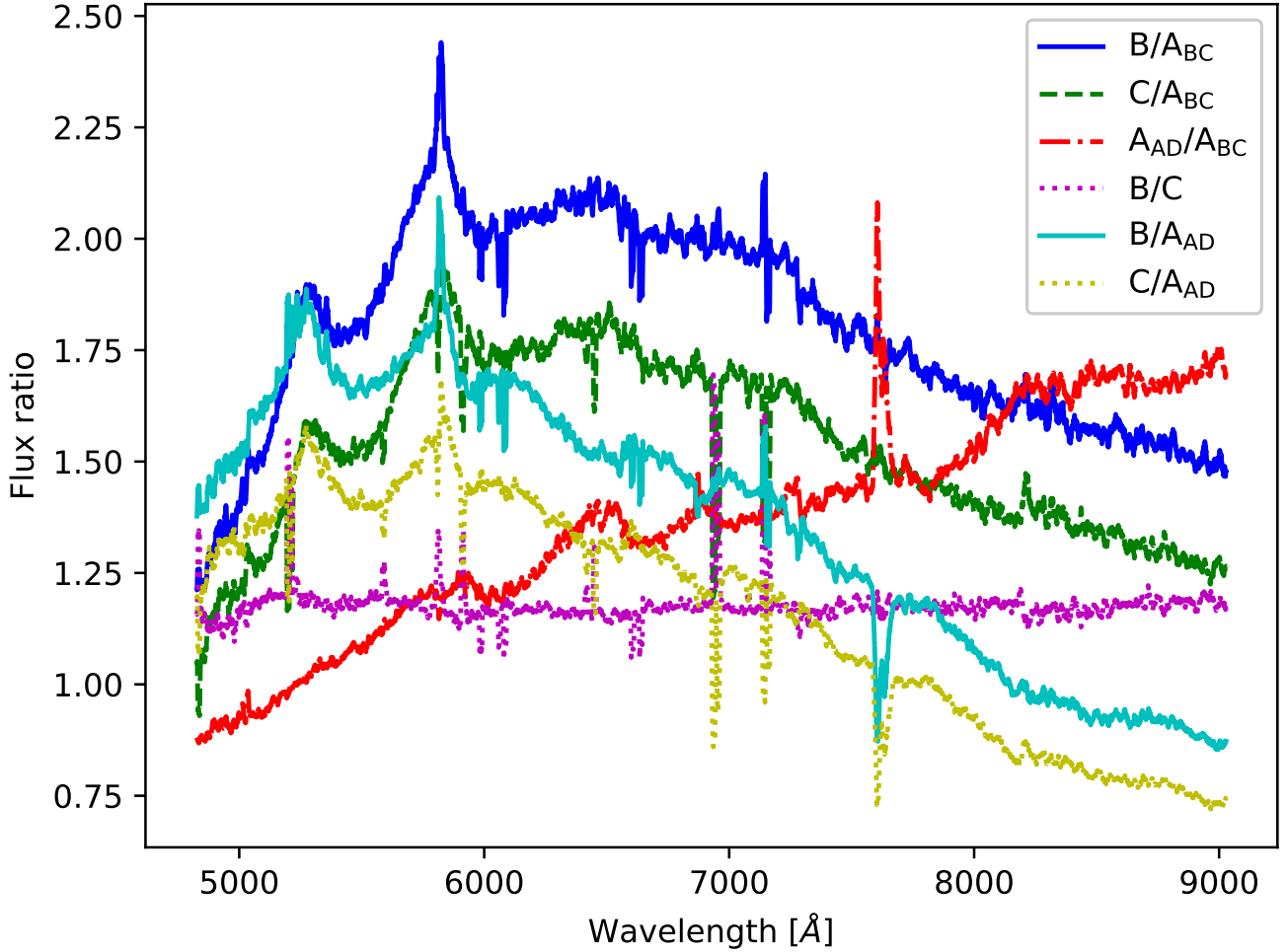


Figure 7. Measured spectral flux ratios in the region 4830 Å–9030 Å, where the measurements are robust. The colors and line styles correspond to those in Fig. 6, except that some flux ratios have been inverted and photometric ratios involving image D have been replaced with spectroscopic ratios of A_{AD} . The spikes correspond to the intrinsic or atmospheric absorption lines in the original spectra.

AST-1238877, the University of Maryland, Eotvos Lorand University (ELTE), the Los Alamos National Laboratory, and the Gordon and Betty Moore Foundation.

This work has made use of data from the European Space Agency (ESA) mission *Gaia* (<https://www.cosmos.esa.int/gaia>), processed by the *Gaia* Data Processing and Analysis Consortium (DPAC, <https://www.cosmos.esa.int/web/gaia/dpac/consortium>). Funding for the DPAC has been provided by national institutions, in particular the institutions participating in the *Gaia* Multilateral Agreement.

Based on observations obtained as part of the VISTA Hemisphere Survey, ESO Program, 179.A-2010 (PI: McMahon). Based on data obtained from the ESO Science Archive Facility under request number cerusu312487.

Some of the data presented herein were obtained at the W. M. Keck Observatory, which is operated as a scientific partnership among the California Institute of Technology, the University of California and the National Aeronautics and Space Administration. The Observatory was made possible by the generous financial support of the W. M. Keck Foundation.

The authors recognize and acknowledge the very significant cultural role and reverence that the summit of Mauna Kea has always had within the indigenous Hawaiian community. We are most fortunate to have the opportunity to conduct observations from this superb mountain.

REFERENCES

- Abolfathi B., et al., 2018, *ApJS*, 235, 42
- Agnello A., Kelly B. C., Treu T., Marshall P. J., 2015, *MNRAS*, 448, 1446
- Agnello A., et al., 2018, *MNRAS*, 475, 2086
- Agnello A., Grillo C., Jones T., Treu T., Bonamigo M., Suyu S. H., 2018, *MNRAS*, 474, 3391
- Agnello A., et al., 2018, *MNRAS*, 479, 4345
- Agnello A., Spiniello C., 2018, *arXiv:1805.11103*
- Aihara H., et al., 2018, *PASJ*, 70, S8
- Arenou F., et al., 2018, *A&A*, 616, A17
- Astropy Collaboration, et al., 2013, *A&A*, 558, A33
- Auger M. W., Treu T., Bolton A. S., Gavazzi R., Koopmans L. V. E., Marshall P. J., Bundy K., Moustakas L. A., 2009, *ApJ*, 705, 1099

- Benítez N., 2000, *ApJ*, 536, 571
- Berghea C. T., Nelson G. J., Rusu C. E., Keeton C. R., Dudik R. P., 2017, *ApJ*, 844, 90
- Bertin E., Arnouts S., 1996, *A&AS*, 117, 393
- Berlind A. A., et al., 2006, *ApJS*, 167, 1
- Bertin E., Mellier Y., Radovich M., Missonnier G., Didelon P., Morin B., 2002, *ASPC*, 281, 228
- Bertin E., 2006, *ASPC*, 351, 112
- Bettoni D., Falomo R., Scarpa R., Negrello M., Omizzolo A., Corradi R. L. M., Reverte D., Vulcani B., 2019, *arXiv*, [arXiv:1902.10964](https://arxiv.org/abs/1902.10964)
- Bonvin V., et al., 2017, *MNRAS*, 465, 4914
- Cardelli J. A., Clayton G. C., Mathis J. S., 1989, *ApJ*, 345, 245
- Chambers K. C., et al., 2016, *arXiv*, [arXiv:1612.05560](https://arxiv.org/abs/1612.05560)
- Chan J. H. H., Suyu S. H., Chiueh T., More A., Marshall P. J., Coupon J., Oguri M., Price P., 2015, *ApJ*, 807, 138
- Chen G. C.-F., et al., 2016, *MNRAS*, 462, 3457
- Claeskens J.-F., Surdej J., 2002, *A&ARv*, 10, 263
- Colless M., et al., 2001, *MNRAS*, 328, 1039
- Croom S. M., Smith R. J., Boyle B. J., Shanks T., Loaring N. S., Miller L., Lewis I. J., 2001, *MNRAS*, 322, L29
- D’Abrusco R., Massaro F., Paggi A., Smith H. A., Masetti N., Landoni M., Tosti G., 2014, *ApJS*, 215, 14
- da Cunha E., et al., 2017, *PASA*, 34, e047
- Delchambre L., et al., 2019, *A&A*, 622, A165
- de Vaucouleurs G., 1948, *AnAp*, 11, 247
- Faber S. M., Jackson R. E., 1976, *ApJ*, 204, 668
- Fabricsius C., et al., 2016, *A&A*, 595, A3
- Falco E. E., et al., 1999, *ApJ*, 523, 617
- Findlay J. R., et al., 2018, *ApJS*, 236, 44
- Flaugher B., et al., 2015, *AJ*, 150, 150
- Flesch E. W., 2015, *PASA*, 32, e010
- Flewelling H. A., et al., 2016, *arXiv*, [arXiv:1612.05243](https://arxiv.org/abs/1612.05243)
- Foreman-Mackey D., Hogg D. W., Lang D., Goodman J., 2013, *PASP*, 125, 306
- Gaia Collaboration, et al., 2016, *A&A*, 595, A1
- Gaia Collaboration, et al., 2018, *A&A*, 616, A1
- Gaia Collaboration, et al., 2018, *A&A*, 616, A14
- Healey S. E., et al., 2008, *ApJS*, 175, 97
- Hennawi J. F., et al., 2006, *AJ*, 131, 1
- Hennawi J. F., et al., 2010, *ApJ*, 719, 1672
- Henstock D. R., Browne I. W. A., Wilkinson P. N., McMahon R. G., 1997, *MNRAS*, 290, 380
- Hewett P. C., Irwin M. J., Foltz C. B., Harding M. E., Corrigan R. T., Webster R. L., Dinshaw N., 1994, *AJ*, 108, 1534
- Holder G. P., Schechter P. L., 2003, *ApJ*, 589, 688
- Hopkins P. F., Hernquist L., Cox T. J., Di Matteo T., Robertson B., Springel V., 2006, *ApJS*, 163, 1
- Hopkins P. F., Hernquist L., Cox T. J., Kereš D., 2008, *ApJS*, 175, 356
- Hunter, J. D., et al. 2007, *Computing in Science & Engineering*, 9, 3, 90-95
- Huo Z.-Y., et al., 2013, *AJ*, 145, 159
- Inada N., et al., 2003, *Natur*, 426, 810
- Inada N., et al., 2008, *AJ*, 135, 496
- Inada N., et al., 2009, *AJ*, 137, 4118
- Inada N., et al., 2010, *AJ*, 140, 403
- Inada N., et al., 2012, *AJ*, 143, 119
- Inada N., Oguri M., Rusu C. E., Kayo I., Morokuma T., 2014, *AJ*, 147, 153
- Jackson N., Rampadarath H., Ofek E. O., Oguri M., Shin M.-S., 2012, *MNRAS*, 419, 2014
- Jean C., Surdej J., 1998, *A&A*, 339, 729
- Jones D. H., et al., 2009, *MNRAS*, 399, 683
- Kayo I., Inada N., Oguri M., Morokuma T., Hall P. B., Kochanek C. S., Schneider D. P., 2010, *AJ*, 139, 1614
- Kayo I., Oguri M., 2012, *MNRAS*, 424, 1363
- Keeton C. R., Kochanek C. S., Falco E. E., 1998, *ApJ*, 509, 561
- Kleinman S. J., et al., 2013, *ApJS*, 204, 5
- Kneib J.-P., Cohen J. G., Hjorth J., 2000, *ApJ*, 544, L35
- Koposov S. E., Belokurov V., Torrealba G., 2017, *MNRAS*, 470, 2702
- Kostrzewa-Rutkowska Z., et al., 2018, *MNRAS*
- Lee C.-H., 2017, *A&A*, 605, L8
- Lee C.-H., 2018, *MNRAS*, 475, 3086
- Lemon C. A., Auger M. W., McMahon R. G., Koposov S. E., 2017, *MNRAS*, 472, 5023
- Lemon, C. A., Auger, M. W., McMahon, R. G., & Ostrovski, F. 2018, *MNRAS*, 479, 5060
- Lemon C. A., Auger M. W., McMahon R. G., 2019, *MNRAS*, 483, 4242
- Lindgren L., et al., 2016, *A&A*, 595, A4
- Lucey J. R., Schechter P. L., Smith R. J., Anguita T., 2018, *MNRAS*, 476, 927
- Maddox S. J., Sutherland W. J., Efsthathiou G., Loveday J., 1990, *MNRAS*, 243, 692
- Magain P., Letawe G., Courbin F., Jablonka P., Jahnke K., Meylan G., Wisotzki L., 2005, *Natur*, 437, 381
- Magnier E. A., et al., 2016a, *arXiv*, [arXiv:1612.05240](https://arxiv.org/abs/1612.05240)
- Magnier E. A., et al., 2016b, *arXiv*, [arXiv:1612.05242](https://arxiv.org/abs/1612.05242)
- McMahon R. G., Banerji M., Gonzalez E., Koposov S. E., Bejar V. J., Lodieu N., Rebolo R., VHS Collaboration, 2013, *Msngr*, 154, 35
- Moffat A. F. J., 1969, *A&A*, 3, 455
- More A., et al., 2016, *MNRAS*, 456, 1595
- Nelder, J. A., Mead. R., 1965, *The Computer Journal* 7, 308-13
- Ochner P., et al., 2014, *ATel*, 6750
- Ofek E. O., Oguri M., Jackson N., Inada N., Kayo I., 2007, *MNRAS*, 382, 412
- Oguri M., et al., 2005, *ApJ*, 622, 106
- Oguri M., et al., 2006, *AJ*, 132, 999
- Oguri M., et al., 2008, *AJ*, 135, 520
- Oguri M., 2010, *PASJ*, 62, 1017
- Oguri M., Marshall P. J., 2010, *MNRAS*, 405, 2579
- Oguri M., et al., 2012, *AJ*, 143, 120
- Oliphant, T. E., 2007, *Computing in Science & Engineering*, 9, 10-20
- Onaka P., Tonry J. L., Isani S., Lee A., Uyeshiro R., Rae C., Robertson L., Ching G., *Proc. 2008, Proc. SPIE*, 7014, 12
- Ostrovski F., et al., 2017, *MNRAS*, 465, 4325
- Ostrovski F., et al., 2018, *MNRAS*, 473, L116
- Peng C. Y., et al., 1999, *ApJ*, 524, 572
- Rubin K. H. R., et al., 2018, *ApJ*, 859, 146
- Rusu C. E., Oguri M., Iye M., Inada N., Kayo I., Shin M.-S., Sluse D., Strauss M. A., 2013, *ApJ*, 765, 139
- Rusu C. E., et al., 2016, *MNRAS*, 458, 2
- Rusu C. E., et al., 2017, *MNRAS*, 467, 4220
- Rusu C. E., Lemon C. A., 2018, *RNAAS*, 2, 187
- Sergeyev A. V., Zheleznyak A. P., Shalyapin V. N., Goicoechea L. J., 2016, *MNRAS*, 456, 1948
- Schechter P. L., Pooley D., Blackburne J. A., Wambsganss J., 2014, *ApJ*, 793, 96
- Schlafly E. F., Finkbeiner D. P., 2011, *ApJ*, 737, 103
- Secrest, N. J., Dudik, R. P., Dorland, B. N., et al. 2015, *ApJS*, 221, 12
- Shanks T., et al., 2015, *MNRAS*, 451, 4238
- Sheinin A. I., Bolte M., Epps H. W., Kibrick R. I., Miller J. S., Radovan M. V., Bigelow B. C., Sutin B. M., 2002, *PASP*, 114, 851
- Sheth, R. K., Bernardi, M., Schechter, P. L., et al. 2003, *ApJ*, 594, 225
- Skrutskie M. F., et al., 1997, *ASSL*, 210, 25
- Sluse D., Chantry V., Magain P., Courbin F., Meylan G., 2012, *A&A*, 538, A99
- Sluse D., et al., 2017, *MNRAS*, 470, 4838
- Spiniello C., et al., 2018, *MNRAS*, 480, 1163

- Surdej J., et al., 1987, *Natur*, 329, 695
 Szabo T., Pierpaoli E., Dong F., Pipino A., Gunn J., 2011, *ApJ*, 736, 21
 Taylor M. B., 2005, *ASPC*, 347, 29
 Tonry J., Onaka P. 2009, in Ryan S., ed., *Proceedings of the Advanced Maui Optical and Space Surveillance Technologies Conference*. The Maui Economic Development Board, Kihei, HI, p. E40
 Treu T., Marshall P. J., 2016, *A&ARv*, 24, 11
 Treu T., et al., 2018, *MNRAS*, 481, 1041
 Weymann R. J., Latham D., Angel J. R. P., Green R. F., Liebert J. W., Turnshek D. A., Turnshek D. E., Tyson J. A., 1980, *Natur*, 285, 641
 Williams P., Agnello A., Treu T., 2017, *MNRAS*, 466, 3088
 Wilson M. L., Zabludoff A. I., Ammons S. M., Momcheva I. G., Williams K. A., Keeton C. R., 2016, *ApJ*, 833, 194
 Wisotzki L., Koehler T., Kayser R., Reimers D., 1993, *A&A*, 278, L15
 Wisotzki, L., Schechter, P. L., Bradt, H. V., Heinmüller, J., & Reimers, D. 2002, *A&A*, 395, 17
 Wong K. C., et al., 2017, *MNRAS*, 465, 4895
 Wright E. L., et al., 2010, *AJ*, 140, 1868-1881
 Yonehara A., Hirashita H., Richter P., 2008, *A&A*, 478, 95
 York D. G., et al., 2000, *AJ*, 120, 1579

separation less than the *WISE* PSF FWHM, and count each of these clusters as one. This reduces the *Gaia*-based sample to ~ 14 million sources, resulting in an AGN fraction of $\sim 4\%$.

APPENDIX B: PREVIOUSLY CONFIRMED OR RULED OUT CANDIDATES

This paper has been typeset from a $\text{\TeX}/\text{\LaTeX}$ file prepared by the author.

APPENDIX A: EXPECTED SAMPLE PURITY FROM THE RELATIVE DENSITY OF *GAIA* AND AGN SOURCES

We start with the complete *Gaia* DR2 source catalogue¹³, where we apply the same automatic selection cuts we used for our sample of candidates. We use a bright magnitude limit of $G \geq 17.5$, slightly brighter than our candidate source companions, and a faint one of $G \leq 20$. While 29 of the 91 candidate source companions are fainter than $G = 20$, we apply this cut because *Gaia* DR2 is still complete at this limit (Arenou et al. 2018), outside the crowded regions excluded by our galactic latitude cut; the completeness is expected to drop towards the limiting magnitude of $G \sim 21$. This reduces the *Gaia* catalogue to ~ 148 million sources. We also apply a color cut of $0 \leq Rp - Bp \leq 1.5$, from Figure 1, as well as the same *Gaia*-based astrometric quantity cuts from Section 2.2. As we did for our candidates, we keep the objects without *Gaia* astrometric quantities or color. This results in ~ 22 million remaining sources.

The Secrest et al. (2015) AGN catalogue is less complete, but not significantly so, with a limiting magnitude of 20 in *g*-band, or about the same in *Gaia* *G*-band¹⁴. We use the Milliquas catalogue (Flesch 2015), which is slightly more complete at this magnitude limit (see Figure 3 in Lemon, Auger, & McMahon (2019)), and includes high-confidence quasars detected in X-ray and radio, in addition to *WISE*. We cross-matched the *Gaia* catalogue after performing the cuts described above with the Milliquas catalogue, resulting in ~ 520000 matches.

Finally, the *Gaia* resolution is much higher than the one of *WISE*, with PSF FWHM $\sim 6''$ (Wright et al. 2010). We use Topcat (Taylor 2005) to identify all objects from the *Gaia*-based catalogue we produced above with relative

¹³ <https://www.astro.rug.nl/~gaia/>

¹⁴ From our 312 candidates, $G - g$ has a distribution with a median of -0.21 and a standard deviation of 0.34

Table B1. Previously confirmed candidates, and those ruled out by *Gaia* data or existing spectroscopy

Name [PS1 J...]	α	δ	#Comp	i	Sep. ["]	Rank	Notes
013459+243049	23.745589	24.513635	2	19.40	3.7	C	$G = 19.60, 20.17$; p-l; two SDSS QSOs at $z=2.093$ and $z=2.104$
014710+463043	26.792452	46.512081	2	15.57	3.2	A	$G = 15.89, 16.18; 16.74, 18.26$; similar color p-l sources; PSJ0147+4630 (quad; Berghea et al. 2017)
024526-055700	41.356685	-5.950128	2	18.67	1.7	C	$G = 19.73, 19.25$; similar color p-l + red inner component; DESJ0245-0556 (double; Agnello et al. 2018)
025934-233802	44.889982	-23.633792	2	19.21	2.7	B	$G = 20.34, 19.37$; p-l + red inner component; PSJ0259-2338 (double; Lemon et al. 2018)
094235+231030	145.645825	23.175133	2	18.87	2.4	C	$G = 19.10, 19.92$; similar color p-l; $z=1.83$ QSO pair (Findlay et al. 2018)
110633-182124	166.639282	-18.356688	2	16.95	3.1	C	$G = 17.07, 18.20$; similar color p-l; HE1104-1805 (double; Wisotzki et al. 1993)
110932+531636	167.384487	53.276552	2	18.71	3.2	C	$G = 18.97, 19.68$; similar color p-l; includes SDSS $z=0.982$ QSO; SQLS QSO pair
113441-210323	173.668953	-21.056307	3	16.81	3.7	A	$G = 17.17, 17.19, 18.94, 17.27$; four p-l sources; 2M1134-2103 (quad; Lucey et al. 2018)
120451+442836	181.210712	44.47659	2	18.84	3.0	B	$G = 18.81, 19.65$; similar color p-l; SQLS QSO at $z=1.84$ and $z=1.14$
120630+433219	181.623684	43.538734	2	18.52	3.0	B	$G = 18.87, 18.84$; similar color p-l + red component; SDSSJ1206+4332 (double; Oguri et al. 2005)
120659-254331	181.744763	-25.725376	2	19.41	2.1	B	$G = 19.97, 20.40$; similar color p-l; both have negligible AEN, pm and p; double, discovered and confirmed independently by C. Lemon, private communication
124614+503049	191.556942	50.513634	2	19.22	2.4	C	$G = 19.31, 19.50$; similar color p-l; SDSS quasar pair $z=2.73, 2.11$
132100+164403	200.246658	16.734072	3	18.51	8.8	B	$G = 18.66, 19.46$; similar color p-l + red component; SDSSJ1320+1644 (double or binary quasar; Rusu et al. 2013)
133713+601208	204.304581	60.202141	2	18.55	3.1	C	$G = 18.68, 19.63$; similar color p-l; $z=1.721, 1.726$ QSO pair (Hennawi et al. 2006)
140515+095930	211.314397	9.991796	2	18.96	1.9	B	$G = 19.38, 20.32$; p-l + extended red; ULAS J1405+0959 (double Jackson et al. 2012)
141818-161008	214.573673	-16.168771	2	18.53	2.4	C	$G = 18.46, 19.33$; similar color p-l; NIQ $z=1.13$ (Lemon, Auger, & McMahon 2019)
143323+600715	218.345158	60.120864	5	19.49	3.7	A	$G = 19.87, 19.99, 20.26$; p-l; SDSSJ1433+6007 (quad; Agnello et al. 2018a)
143351+145007	218.462505	14.835308	2	18.90	3.3	C	$G = 18.99, 19.35$; similar color p-l; $z=1.51$ QSO pair (Findlay et al. 2018)
151539+151135	228.910562	15.193168	2	17.94	2.0	C	$G = 18.03, 18.42$; similar color p-l; SDSSJ1515+1511 (double; Inada et al. 2014)
153725-301017	234.355599	-30.171336	4	19.12	3.1	A	$G = 20.32, 20.22, 20.44$; four p-l + inner red component; (quad; Delchambre et al. 2019 ; Lemon, Auger, & McMahon 2019)
160600-233322	241.500981	-23.556046	3	17.96	2.9	C	$G = 18.85, 18.97, 19.33, 19.61$; p-l + red component; PSJ1606-2333 (quad; Lemon et al. 2018)
172145+884222	260.43637	88.706169	2	17.33	2.3	B	$G = 18.18, 18.33$; similar color; PSJ1721+8842 (quad; Lemon et al. 2018)
203238-235822	308.157206	-23.972856	2	18.75	2.0	C	$G = 19.12, 19.26$; similar color p-l; $z=1.64$ NIQ (Lemon et al. 2018)
215316+273235	328.31765	27.543058	2	18.69	3.6	C	$G = 18.72, 19.69$; similar color p-ls; quasar pair (Sergeyev et al. 2016)
221208+314417	333.033412	31.73809	2	19.27	2.6	C	$G = 19.28, 19.97$; two similar color p-l + red component; (double; Lemon, Auger, & McMahon 2019)
000823+031342	2.094362	3.228219	2	17.70	3.2	C	p-l; PB 5757 (star), large pm
001313-152007	3.302628	-15.335383	2	16.82	1.9	C	similar color p-l; companion has large pm
002605+401519	6.522825	40.255255	2	17.85	2.3	C	p-l; companion has large pm
002719+300336	6.827338	30.059894	2	17.90	3.0	C	similar color p-l; companion has large pm
004346+282715	10.942056	28.454297	2	17.58	3.3	C	point sources; bright component has large pm and p
004446+472400	11.192613	47.399741	2	18.13	3.3	C	similar color p-l; companion has large pm
005801-231711	14.502676	-23.286411	2	17.82	3.1	C	similar color p-l; one component has large AEN
011305+454905	18.269259	45.818058	2	17.60	1.7	C	similar color p-l; companion has large pm
011639+405252	19.163546	40.881125	2	18.72	1.3	C	similar color p-l; includes SDSS $z=1.86$ QSO; one component has large p
015109+315521	27.786404	31.922389	2	18.11	3.1	C	includes galaxy (Ochner et al. 2014); companion has large pm
020122+212637	30.340775	21.443685	2	17.45	3.6	C	similar color p-l; SQLS candidate; companion has large pm
020649+803347	31.703677	80.563065	2	17.36	2.2	C	similar color p-l; companion has large pm and p
020722+374720	31.843188	37.788868	2	16.60	2.2	C	similar color p-l + extended; companion has large pm and p
024414-073747	41.059791	-7.629853	2	19.75	1.4	C	p-l; includes $z=0.319$ galaxy (Szabo et al. 2011); companion has no Gaia pm and p
024722-172547	41.843352	-17.429683	2	18.67	1.6	C	similar color p-l; companion has large pm
025339+070440	43.414166	7.077896	2	18.17	2.8	C	similar color p-l; companion has large pm
025644+394153	44.183373	39.697932	2	19.28	2.4	C	similar color p-l; companion has large pm
034955-071723	57.479613	-7.289607	2	16.12	2.5	C	p-l; companion has large pm and p
035119-182302	57.829409	-18.383904	2	16.92	1.8	C	p-l; companion has large pm and p
041304+155206	63.266175	15.868444	2	17.60	3.5	C	similar color p-l; companion has large pm
043324-111537	68.348462	-11.260161	2	18.31	2.7	C	similar color p-l; companion has large pm
045230-295335	73.125436	-29.893138	2	15.36	2.0	B	similar color p-l + extended? star+interacting galaxy+QSO HE0450-2958 (Magain et al. 2005)
051139-035102	77.911071	-3.850553	2	19.02	2.9	C	similar color p-l; QSO+other (Lemon et al. 2018); both negligible AEN, pm and p
052131+730136	80.380313	73.026614	2	17.55	3.0	C	p-l; companion has large pm and p
052419-065727	81.077162	-6.957592	2	16.98	1.8	C	p-l; companion has large pm
052833+042744	82.136604	4.462234	2	16.72	1.9	C	p-l; companion has large pm
053733+815634	84.386019	81.942802	2	18.72	3.2	C	similar color p-l; companion has large pm
054335-152624	85.894214	-15.439864	2	17.63	2.8	C	p-l; companion has large pm
061050-201839	92.710135	-20.310915	2	18.37	2.8	C	p-l; companion has large pm
061911-295857	94.796622	-29.982405	3	18.70	2.3	C	different color p-l; outer component has large AEN and pm; included in the Delchambre et al. (2019) Gaia clusters catalogue
062529-285546	96.371981	-28.929452	2	18.25	3.0	C	p-l; companion has large pm
063724+434603	99.34909	43.767531	3	16.9	5.3	C	similar color p-l (companion has large pm and p) + red inner component
065513+850519	103.804667	85.088737	3	17.50	4.5	B	similar color p-l (companion has large pm) + red inner component (large AEN); included in the Delchambre et al. (2019) Gaia clusters catalogue

Table B1 – continued

Name [PS1 J...]	α	δ	#Comp	i	Sep. ["]	Rank	notes
072846+420701	112.190784	42.116988	2	16.79	3.9	C	similar color p-l; includes SDSS z=1.120 QSO; SQLS candidate; companion has large pm and p
072850+570125	112.206878	57.02358	2	16.03	3.5	C	p-l; includes z=0.426 Seyfert 1 (Henstock et al. 1997); companion has large pm and p
074242+651038	115.673761	65.177097	2	15.17	2.0	C	consistent with single extended source; Mrk 78 (Seyfert 2); no Gaia data
074555+181818	116.478082	18.304882	2	17.80	2.5	C	p-l; includes SDSS z=1.060 QSO; SQLS candidate; companion has large pm
080938+275648	122.407538	27.946714	2	17.09	3.1	C	similar color p-l; includes SDSS z=0.406 QSO; companion has large pm and p
081130+255541	122.876253	25.927955	2	18.96	2.7	C	p-l; companion has large pm
082218+665957	125.574156	66.999183	2	18.61	3.0	C	similar color p-l; QSO+other (Lemon et al. 2018); both negligible AEN, pm and p
082353-085114	125.970487	-8.853931	2	16.88	2.2	C	similar color p-l; companion has large pm and p
082442+592409	126.176996	59.402484	2	17.77	3.1	C	similar color p-l; companion has large pm
083229+563235	128.119012	56.542997	3	18.76	3.0	C	similar color p-l (companion has large pm) + inner red component; includes SDSS z=0.683 QSO; SQLS QSO+star
084441+334909	131.16938	33.819226	2	18.28	2.9	C	similar color p-l; includes SDSS z=1.425 QSO; SQLS candidate; companion has large pm
084513+543422	131.302961	54.57264	2	18.51	1.4	C	similar color p-l; includes SDSS z=1.290 QSO; SQLS QSO+star (large pm)
085055-052735	132.72728	-5.459747	2	19.11	2.0	C	similar color p-l; companion has large pm
085838-152907	134.656619	-15.485172	2	17.27	2.5	C	similar color p-l; companion has large pm
090852+304332	137.215844	30.725594	2	18.51	2.1	C	p-l; includes SDSS z=0.399 Seyfert 1; companion has large pm
091453-265223	138.722422	-26.873106	2	17.80	2.4	C	similar color p-l; companion has large pm
091746-160623	139.443706	-16.106479	4	18.41	2.3	C	similar color p-l; companion has large pm; included in the Delchambre et al. (2019) Gaia clusters catalogue
092016-063144	140.064718	-6.529	2	18.16	2.7	C	similar color p-l; companion has large pm
092438-012845	141.157105	-1.479089	2	17.99	3.0	C	similar color p-l; includes SDSS z=2.446 QSO; companion has large pm
092718+211357	141.826656	21.232549	2	17.47	2.3	C	p-l; includes SDSS z=1.851 QSO; SQLS candidate, no lensing object; companion has large pm
094115+305810	145.314113	30.969479	2	19.29	2.3	C	similar color; SQLS z=1.193 QSO+blue galaxy
094437-263355	146.154045	-26.565394	2	16.77	2.3	C	similar color; includes Seyfert 1 galaxy at z=0.142 (Jones et al. 2009) companion has large pm
094903+280022	147.264552	28.006127	2	18.79	1.2	C	similar color p-l; SQLS QSO+star
100450+773753	151.208619	77.63132	2	19.05	1.9	C	similar color p-l; companion has large pm
102803-153028	157.011143	-15.507813	3	19.60	4.5	B	p-l + red inner component (large pm)
102813+171902	157.054777	17.317297	2	18.53	1.9	C	p-l; only one component has Gaia p and pm, large pm
104704-241459	161.765852	-24.249719	2	16.95	2.8	B	similar color p-l (companion has large pm) + red inner component
105852-275715	164.715138	-27.954048	2	18.01	2.4	C	similar color p-l; companion has large pm
111524-042218	168.848654	-4.371723	2	18.60	2.7	C	similar color p-l; includes galaxy at z=0.209 (Colless et al. 2001); no Gaia p and pm, large AEN for companion
113431+111918	173.628607	11.321701	2	18.49	1.6	C	similar color p-l; large companion pm; z=1.62 QSO+star Ostrovski et al, in prep.
114214-075619	175.556357	-7.93867	2	18.93	3.4	C	similar color p-l; companion has large pm
115443-224432	178.680182	-22.742147	2	17.75	2.4	B	similar color p-l; companion has large pm
115541+131105	178.919792	13.184774	2	17.52	2.4	B	similar color p-l; companion has large pm
115957+644406	179.987136	64.735049	2	18.77	3.1	C	similar color p-l; includes SDSS z=1.61 QSO; companion has large pm
123441+341000	188.672008	34.166556	2	18.29	2.2	C	similar color p-l; includes SDSS z=1.429 QSO, SQLS candidate; companion has large pm
123559-023503	188.993809	-2.58423	2	17.78	3.0	C	similar color p-l; SDSS z=2.062 QSO+star, SQLS candidate
130738+640252	196.907012	64.047899	2	18.17	3.5	C	similar color p-l; companion has large pm
131425+181232	198.605024	18.208753	2	19.46	2.5	C	p-l; companion has large pm
132223+512017	200.595155	51.338029	2	18.29	2.7	C	similar color p-l; includes SDSS z=1.772 QSO; SQLS candidate; companion has large pm
132405+282334	201.022027	28.392698	2	18.54	2.1	C	similar color p-l; includes SDSS z=0.904 QSO; SQLS candidate, no lensing object; companion has large pm
132853+261501	202.222599	26.250248	2	18.91	2.6	C	similar color p-l; SQLS candidate; SDSS z=1.522 QSO + star; companion has large pm
132916+414554	202.31656	41.765054	2	17.59	2.8	C	similar color p-l; companion has large pm
133543-294239	203.927943	-29.710967	2	18.50	2.4	C	p-l; companion has large pm
134222-261001	205.593589	-26.166945	2	18.30	2.9	C	similar color p-l; companion has large pm
134539-262819	206.411024	-26.471915	2	17.82	2.6	C	similar color p-l; companion has large pm
134626+045245	206.609217	4.879294	2	18.73	2.7	C	similar color p-l; companion has large pm
134941+011054	207.420114	1.181594	2	16.55	2.2	C	similar color p-l; includes SDSS star
140610-250809	211.540001	-25.135907	2	17.88	2.9	B	similar color p-l; companion has large pm
141349+475113	213.452222	47.853718	2	18.55	3.0	C	similar color p-l; includes SDSS z=2.175 QSO; SQLS candidate, no lensing object; companion has large pm
141432-052951	213.631386	-5.49754	2	19.17	2.2	C	similar color p-l; companion has large pm
142040+122507	215.16569	12.418669	2	18.31	3.1	C	similar color p-l; includes SDSS z=2.252 QSO; companion has large pm
142402+710911	216.008966	71.152985	2	18.70	2.9	C	similar color p-l; companion has large pm
142609-210327	216.538323	-21.057381	2	19.44	2.8	C	similar color p-l; companion has large pm
143153-094341	217.972653	-9.727974	3	18.56	5.8	B	p-l (companion has large pm) + red inner component
143154+530033	217.973863	53.009266	3	18.09	4.3	C	p-l; includes SDSS z=1.389 QSO + star; third component has large pm included in the Delchambre et al. (2019) Gaia clusters catalogue
143245-273713	218.188947	-27.620192	2	17.78	3.0	C	similar color p-l; companion has large pm
144145+023743	220.437914	2.628697	2	19.13	1.1	C	similar color p-l; SQLS z=1.160 QSO+star
144245+041619	220.689582	4.271996	2	19.27	3.0	C	p-l; includes SDSS z=2.012 QSO; SQLS candidate; companion has large pm
144303+260329	220.763978	26.058137	2	17.98	3.5	C	similar color p-l; includes SDSS z=0.257 Seyfert 1; companion has large pm

Table B1 – *continued*

Name [PS1 J...]	α	δ	#Comp	i	Sep. ["]	Rank	notes
145115+052936	222.813312	5.493197	2	16.20	2.3	C	similar color p-l; includes SDSS $z=2.052$ QSO; SQLS candidate; companion has large pm
145232-052947	223.134353	-5.496432	2	18.04	2.9	C	p-l + red inner component; companion has large pm
145647-091751	224.197573	-9.297562	2	17.99	3.0	C	similar color p-l; companion has large p and pm
150925+113851	227.35556	11.647604	2	19.37	2.5	C	similar color p-l; includes SDSS star; only one component has Gaia p and pm, negligible values
151044-074043	227.684808	-7.678621	2	18.27	2.5	C	similar color p-l; companion has large pm
151205+182706	228.018788	18.451666	2	17.76	2.5	C	similar color p-l; companion has large pm
151237+553901	228.15381	55.650295	2	19.01	1.9	C	similar color p-l; includes SDSS $z=1.363$ QSO; SQLS QSO+star
151527-203609	228.862483	-20.602366	2	17.84	2.9	C	p-l; companion has large pm
151832+343325	229.632917	34.557016	2	18.87	3.0	C	similar color p-l; includes SDSS $z=1.672$ QSO; SQLS candidate; companion has large pm
151858-022443	229.74139	-2.411924	3	16.9	3.3	B	p-l; inner component has large pm, the other two have negligible AEN, p and pm
151918+094205	229.826754	9.701277	2	18.11	3.7	C	similar color p-l; companion has large pm
152005+195038	230.021454	19.843884	3	18.73	1.4	C	similar color; a single companion has Gaia data (only AEN, large)
152050+263741	230.209019	26.627994	2	18.93	2.1	C	p-l; includes SDSS $z=1.365$ QSO; SQLS candidate candidate; companion has large p and pm
152444+054628	231.182118	5.77438	2	17.68	3.7	C	similar color p-l; includes SDSS $z=1.445$ QSO; SQLS candidate; companion has large pm
153223-291257	233.094882	-29.215933	2	19.05	1.8	C	similar color p-l; companion has large pm
153311-001509	233.296204	-0.252541	3	19.49	4.0	C	similar colors; only one, outer component has Gaia data, large pm, the others are galaxies
153510+082347	233.79015	8.396438	2	18.77	2.5	C	p-l; third component? includes SDSS $z=1.953$ QSO; SQLS candidate; companion has large pm
154226-023456	235.610402	-2.582135	2	18.74	3.1	C	similar color p-l; companion has large pm
154726-153237	236.857051	-15.543614	2	17.96	2.7	C	similar color p-l; companion has large pm
160138+172852	240.407737	17.48102	3	17.80	5.6	C	similar color p-l (one component has large pm) + red inner components (large pm); includes SDSS $z=2.239$ QSO
160927+175431	242.361547	17.90869	2	17.67	2.6	C	similar color p-l; includes SDSS $z=1.993$ QSO; SQLS candidate; companion has large pm
161008+234837	242.533565	23.810394	2	19.14	3.0	C	similar color p-l; companion has large pm
161657-170647	244.235836	-17.113065	2	18.12	2.6	C	similar color p-l; companion has large pm
161722-230546	244.340087	-23.096165	2	18.80	1.8	C	similar color p-l; QSO+star (Lemon et al. 2018)
161841+301311	244.669946	30.2196	2	17.61	2.5	B	similar color p-l; includes SDSS $z=1.403$ QSO; companion has large pm
161931+162123	244.878602	16.356363	2	19.08	2.6	C	similar color p-l; includes SDSS $z=2.455$ QSO; companion has large pm
162417+064152	246.070533	6.697785	2	18.44	2.4	C	similar color p-l; companion has large pm
163113-171407	247.804331	-17.235305	2	17.59	3.0	C	similar color p-l; companion has large pm
163533+205229	248.886788	20.87476	2	18.49	2.1	C	similar color p-l; companion has large pm
163614+094317	249.056552	9.721352	2	19.21	2.2	C	similar color p-l; companion has large pm
163959-210652	249.995488	-21.114331	2	18.84	1.7	C	similar color p-l; companion has large pm
164304+754120	250.765894	75.688987	2	18.08	3.5	C	similar color p-l; companion has large pm
164552+152025	251.465796	15.340377	2	19.04	2.2	B	similar color p-l; companion has large pm
170002+250336	255.009344	25.060094	3	18.50	4.7	C	similar color p-l; 2 components have large pm
170024+005815	255.099997	0.970862	2	16.44	1.6	C	similar color p-l; companion has large pm
170514+331637	256.307089	33.276899	2	18.98	2.2	C	similar color p-l; includes SDSS $z=2.224$ QSO; companion has large pm
170516+251533	256.316261	25.259123	2	18.34	2.1	C	similar color p-l; companion has large pm
170602+270515	256.509411	27.087583	2	17.31	2.3	C	similar color; one component has large pm, the other one large AEN
170817+325311	257.072403	32.886393	2	18.38	2.1	C	similar color p-l; companion has large AEN and pm
170858-030510	257.240718	-3.086224	2	17.60	2.5	C	p-l; companion has large pm
170943+334304	257.427474	33.717724	2	19.13	3.3	C	similar color p-l; both have large pm
171102+292951	257.757094	29.497482	2	17.92	2.2	C	similar color p-l; includes SDSS $z=1.329$ QSO; SQLS candidate; companion has large pm; no lensing object
172634+530300	261.639624	53.050095	2	18.76	1.3	C	similar color p-l; includes white dwarf (Kleinman et al. 2013)
173152+743615	262.968365	74.604272	3	16.60	5.9	C	p-l (one has large p and pm) + red inner component
173316+084954	263.31709	8.831643	2	17.78	2.4	C	similar color p-l; companion has large pm
173509+094022	263.787393	9.672832	2	17.07	2.4	C	similar color p-l; companion has large pm
173703+271724	264.262899	27.290003	2	18.37	2.5	C	p-l; companion has large pm
173820+041756	264.581302	4.298981	2	18.88	2.0	C	similar color p-l; companion has large pm
173905+120306	264.77013	12.051664	2	17.77	2.8	C	similar color p-l; companion has large pm
173915+112257	264.813269	11.382484	2	18.84	3.4	C	similar color p-l; companion has large pm
174006+221101	265.024352	22.183576	2	17.45	1.8	C	similar color p-l; includes $z=1.406$ QSO (Healey et al. 2008); companion has large pm
174154+333616	265.474939	33.604416	3	16.54	8.5	C	p-l; outer components have large p and pm
174213+402717	265.55245	40.454758	2	18.30	3.1	C	similar color p-l; companion has large pm
175243+093822	268.179389	9.639313	2	18.29	2.6	C	similar color p-l; companion has large pm
175826+191732	269.608868	19.292361	2	17.57	2.5	C	similar color p-l; companion has large pm
180257+244143	270.737205	24.695406	3	17.27	4.3	C	similar color p-l (one companion has large pm) + red central component
180901+160103	272.254121	16.017515	2	18.59	3.1	C	similar color p-l; companion has large pm
181045+742546	272.686785	74.429515	2	18.39	2.0	C	similar color p-l; companion has large pm
181400+705410	273.499637	70.902881	2	17.69	2.4	C	similar color p-l; companion has large pm
182159+275657	275.494183	27.949111	2	18.43	2.4	C	similar color p-l; companion has large pm
182301+500140	275.753046	50.027664	2	17.91	2.0	C	p-l; companion has large pm
183204+491637	278.015957	49.276889	2	18.06	1.9	C	similar color p-l; companion has large pm
183852+520350	279.718445	52.063814	2	18.13	3.1	C	p-l; companion has large pm
183916+454103	279.818168	45.684238	2	18.70	3.0	C	similar color p-l; 4C 45.38, $z=0.958$ QSO; companion has large pm
184256+442102	280.733259	44.350567	2	18.33	3.1	C	similar color p-l; companion has large pm
185008+441126	282.533367	44.190435	2	17.64	2.7	C	similar color p-l; companion has large pm
185824+475553	284.600174	47.931329	3	18.54	3.6	B	p-l (one component has large pm), red inner component
190003+522319	285.012245	52.388677	3	18.18	2.8	C	similar color p-l (one component has large pm) + red inner component
190433+575031	286.139132	57.841829	2	19.00	3.2	C	similar color p-l; companion has large pm

Table B1 – continued

Name [PS1 J...]	α	δ	#Comp	i	Sep. ["]	Rank	notes
192457+492126	291.239533	49.357218	2	18.71	2.8	C	similar color p-l; companion has large pm
195629-064134	299.121219	-6.692813	2	19.12	1.6	C	similar color p-l; companion has large pm
200550-030100	301.456704	-3.016733	2	18.49	3.7	C	similar color p-l; companion has large pm
201810-022908	304.540147	-2.485511	2	18.25	1.8	C	similar color p-l; companion has large pm
202339-290706	305.91091	-29.1182	2	17.93	2.0	C	similar color p-l; companion has large pm
203106-122005	307.776472	-12.334677	3	17.59	3.1	C	similar color p-l (one component has large pm) + red companion
204541+122718	311.419538	12.454995	2	17.86	3.0	C	similar color p-l; companion has large pm
204628-120049	311.615311	-12.01355	2	19.12	1.9	C	similar color p-l; companion has large pm
210519+161334	316.330544	16.226221	2	18.71	1.7	C	similar color p-l; companion has large pm
210820+122340	317.08394	12.394343	2	17.89	1.8	C	similar color p-l; one component has large p
211017+050707	317.571284	5.118593	2	18.60	2.8	C	similar color p-l; companion has large pm
211945+153713	319.938477	15.620234	2	17.58	2.9	C	similar color p-l; companion has large pm
212753+085302	321.972353	8.883872	2	18.50	2.2	C	similar color p-l; companion has large pm
213147-030935	322.946983	-3.159735	3	18.52	6.9	C	similar color p-l (one has large pm) + extended inner component
213707+124621	324.279402	12.772593	2	18.67	1.8	C	similar color p-l; BL Lac (D'Abrusco et al. 2014); companion has large pm
214102+265252	325.257922	26.881249	2	17.78	2.8	C	p-l; companion has large pm
214210+255233	325.543115	25.875914	2	16.95	2.4	C	similar color p-l; companion has large pm
214248+290427	325.698926	29.074187	2	17.38	3.6	C	similar color p-l; X-ray source (D'Abrusco et al. 2014); companion has large p and pm
214605+264507	326.52051	26.75202	2	19.2	2.3	C	similar color p-l; companion has large pm
215502+190303	328.756839	19.050739	2	16.86	2.1	B	similar color p-l; QSO+star (NTT run 0100.A-0297(A), PI. T. Anguita)
220822-142722	332.093734	-14.455987	2	17.25	2.1	C	similar color p-l; companion has large p and pm
222238+354225	335.656449	35.707081	2	18.30	2.1	C	similar color p-l; companion has large pm
222611-282413	336.547769	-28.403508	2	19.18	2.7	C	similar color p-l; includes z=0.016 galaxy (Maddox et al. 1990); companion has large pm
223604+221604	339.015242	22.267863	2	17.98	3.1	C	similar color p-l; companion has large pm
223713+245120	339.304497	24.855563	2	18.26	1.7	B	similar brightness p-l; companion has large pm
223831+140027	339.629583	14.007554	2	19.50	3.1	B	similar color p-l + extended? HS 2236+1344 (blue compact galaxy); both have large AEN, no other Gaia data
230258-281314	345.740301	-28.220566	2	18.24	1.7	C	similar color p-l; QSO+star (Lemon et al. 2018)
231209+203543	348.036702	20.595139	2	19.16	3.1	C	p-l + extended; companion has large pm
231313+194722	348.302961	19.7895	2	17.63	3.2	C	similar color p-l; companion has large pm
231445+303530	348.687176	30.591695	2	17.20	3.0	C	p-l; companion has large p and pm
232837+435308	352.152836	43.885431	2	17.33	2.1	B	p-l; companion has large pm
233611-093523	354.043989	-9.589647	2	15.63	4.1	C	similar color p-l; companion has large p and pm
233700+180520	354.249022	18.088753	2	17.63	3.7	C	p-l; companion has large pm
234155+132902	355.480568	13.483904	2	18.82	3.2	C	similar color p-l; includes SDSS z=0.729 QSO; companion has large pm
235351-053956	358.462667	-5.665505	3	16.5	6.2	B	similar color p-l (companion has large p and pm) + red inner component; QSO+star (Williams, Agnello, & Treu 2017)

The systems above the horizontal line are confirmed lenses or quasar pairs. The ones below are candidates ruled out either due to their *Gaia*-based properties, or due to spectroscopic results from the literature. The table structure is the same as in Table 1. “NIQ” stands for nearly identical quasars.